

In-Flight Flow Visualization Results Of The F-106B With A Vortex Flap

Jay M. Brandon, James B. Hallissy,
Philip W. Brown, John E. Lamar

*NASA Langley Research Center
Hampton, VA USA 23681*

Symposium on Advanced Flow Management
Part A – Vortex Flow and High Angle of Attack
May 7-11, 2001
Loen, Norway

North Atlantic Treaty Organization
Research and Technology Organization
Applied Vehicle Technology Panel (AVT)

IN-FLIGHT FLOW VISUALIZATION RESULTS OF THE F-106B WITH A VORTEX FLAP

Jay M. Brandon, James B. Hallissy, Philip W. Brown, John E. Lamar
NASA Langley Research Center, Hampton, VA USA 23681

SUMMARY

Surface and off-surface flow visualization techniques were used to visualize the three-dimensional vortex flows on the F-106 aircraft with vortex flaps installed. Results at angles of attack between 9° to 18° and Mach numbers from 0.3 to 0.9 are presented. A smoke flow vapor screen technique was used to document leading-edge vortex paths and sizes, while an oil flow technique was employed to provide detailed information on reattachment and separation line locations and other flow details. Results were obtained for two vortex flap deflection angles, 30° and 40° . Flow visualization revealed the existence of a multiple vortex system that had not previously been seen in subscale tests or predicted for this configuration. The vortex flap generated a leading-edge vortex system that reattached near the flap hinge over a wide angle of attack range. In addition to the primary vortex, flow visualization revealed the presence of several distinct vortices which traced a path from the vortex flap and then over the wing.

INTRODUCTION

The vortex flap concept repositions the wing leading-edge vortices such that they move from the wing onto the flap surface. The resulting induced suction pressures on the forward facing flap produce a thrust component that reduces drag. This concept has been examined in many experimental and theoretical studies¹⁻⁴ and has been found to be an effective method for improving the performance of highly swept configurations at maneuver lift coefficients. This technology shows promise in improving maneuvering performance of supersonic-cruise fighter configurations, as well as improving the take-off performance of high-speed civil transport airplane designs. As a result, considerable research has been conducted to develop analytical tools for the design of efficient and highly effective vortex flaps⁵.

A flight validation program was conducted at the NASA Langley Research Center using an F-106B testbed aircraft to verify the design tools and expected performance benefits for the vortex flap concept. The primary emphasis of the flight program was the measurement of pressure profiles along the vortex flap and wing to provide verification of design techniques. In addition, limited performance flight testing was accomplished with and without the vortex flap to obtain indications of performance increments which were obtained due to the flap. The flap was flown at two deflection angles as part of the validation process.

Flow visualization data were obtained to verify the structure of the flowfield, and to aid in the interpretation of the flight test data. Off-surface flow visualization using a vapor screen system similar to that used previously⁶ revealed an unanticipated flow field consisting of a multiple vortex system in addition to the leading-edge vortex positioned along the leading-edge flap. To further study the flow characteristics, surface flow visualization using oil coatings on the wing and flap were conducted. This report summarizes the flowfield characteristics observed with the vortex flap configurations over a wide range of angle of attack, Mach number, and sideslip.

TEST AIRPLANE AND TEST TECHNIQUES

Airplane Description

The F-106B airplane used for this study is a two-seat version of a supersonic all-weather fighter/interceptor built by Convair in 1958. The airplane is powered by a Pratt and Whitney J-75-P-17 afterburning turbojet engine. The design features a 60° sweep delta wing planform (aspect ratio 2.20), with an area-ruled fuselage. The controls consist of elevons for pitch and roll control, and a rudder for yaw control, all using a conventional hydraulic non-reversible flight control system. The airplane wings were painted black to improve contrast during the flow visualization tests. The airplane was modified by the addition of vortex flaps to the leading edges of the wing. The vortex flap was ground adjustable to

deflections of 20, 30, 40, and 50 degrees. The flaps were attached to the baseline airplane leading edge, and were made as a series of segments as shown in figure 1. The segments were required to allow for wing bending during flight, and were made to prevent airflow between segments and with as small as geometric discontinuities along the flap surface as possible. The vortex flap flight test validation program flew with the flaps set to 30° and 40°. The test airplane was equipped with a flight test noseboom for accurate air data information, and extensive instrumentation for gathering surface pressure information over the right wing and flap, and to obtain standard flight test parameters of aircraft states and control positions in flight. These data were telemetered to a ground monitoring station real-time during the test flights, and recorded onboard using fm tapes. The airplane was fitted with a propylene glycol smoke generation system, and a rotating light sheet system which could illuminate a large extent of the wing surface. Surface oil flow testing was also conducted inflight. The left wing was used for all on and off-surface flow visualization tests. The right wing was outfitted to obtain surface pressure measurements.

Smoke Injection System

The flow visualization system (fig 2) consisted of two video cameras (one located on the engine intake, and one near the aircraft centerline aft of the canopy), a propylene glycol smoke generation system which consisted of a storage tank, vaporizer, heated hose, and smoke probe, and a rotating light sheet. The three gallon propylene glycol reservoir gave 45 minutes of smoke at a nominal pump speed. The pump speed could be controlled from the rear cockpit to produce the desired volume of smoke.

Light Sheet and Video Recording Systems

The light sheet package could be mounted on top of the airplane fuselage and consisted of a mercury-arc light which was converted to a light sheet using a .048" slit with knife-edges. The light sheet was directed over the wing using a system of lenses and a mirror. The light sheet azimuth was controllable from the rear cockpit and could illuminate portions of the wing from angles of 40° to 160° as shown in figure 3. The light sheet did not illuminate the surface of the flap due to the deflection angle of the flap. The rear cockpit was equipped with a video monitor that displayed the in-flight selected video camera data with time, angle of attack, and light sheet position superimposed at the bottom of the screen. These data were recorded on a super-VHS format video recorder, while the raw camera images for each camera were recorded with time code information separately on standard VHS recorders.

Vapor Screen Test Technique and Flight Procedures

Vapor screen flow visualization tests were conducted at night during periods of very low moon illumination. Test conditions for these data ranged from 5000 feet to 37000 feet altitude at 1-g flight conditions. Flight test points were also obtained at elevated g conditions to achieve desired α /Mach combinations. These elevated g flight conditions were obtained at Mach numbers up to 0.95 and g levels up to 4 g's for the vortex flap airplane. The angle of attack range included in these tests was from $\alpha=7^\circ$ to $\alpha=18^\circ$.

Surface Flow Test Technique and Flight Procedures

On-surface flow visualization was conducted using both oil flow and tuft techniques. The oil studies used a mixture of clear mineral oil, titanium dioxide, and oleic acid to provide white oil for contrast with the wing, which was painted black. The oil mixture was painted on the wing prior to take-off. One angle of attack condition was obtained per flight using this method. The oil flow portion of the flight typically was complete 10 minutes after takeoff.

Tufts were also used for surface flow visualization on the wing and vortex flap. The tufts were plastic cones, approximately 3" long secured to the wing with string and tape.

Surface flow visualization results were obtained primarily at 1-g flight at low altitudes (below 15,500 ft) with a chase plane in formation to obtain photographs of the oil or tuft patterns. Data were obtained from $\alpha=8^\circ$ to $\alpha=18^\circ$.

VORTEX FLAP CONCEPT

The concept of the vortex flap is to reposition the leading edge vortex system which normally develops over the wing at high angles of attack for high swept wings onto a forward facing flap surface. This results in a reduction of induced drag due to a thrust component derived from the vortex low pressure on the flap. The idealized flow conditions are sketched in figure 4. The vortex systems utilized in this concept are much weaker and less persistent than the familiar vortex systems seen in highly swept wing or strake planforms at high angles of attack, and one aspect of this research was to investigate how these vortex systems would behave under realistic flight conditions.

Extensive wind tunnel and analytical work has been conducted in the development of design methodologies of vortex flaps. The flap flown on the F-106B was designed using methods of ref 5. The design process was used to design the flap for a leading-edge vortex reattachment point on the flap/wing hinge line at maneuvering lift coefficients.

Wind tunnel test results conducted on various configurations (refs 7 - 9) validated the design methodology. Tests were also conducted on the F-106B with vortex flaps and also verified the design technique. Each of these tests showed a single leading-edge vortex system which was manipulated by the addition of vortex flaps. Proper design of the flap geometry resulted in the reattachment of the flow to occur near the flap hingeline. At high angles of attack, the vortex would migrate off the flap, over the wing surface, and finally the vortex would burst.

FLIGHT TEST RESULTS

The intersection of the camera field of view and the light sheet provided the vapor screen image data. Because flights were conducted on moonless nights, the outline of the wing is not visible in the data. By using a resectioning technique which involved calibration of the camera and light-sheet systems using known points on the wing, it was possible to calculate the position of the images in the vapor screen data relative to aircraft coordinates. This information could then be used to track the movement of the vortices with angle of attack, and also allowed the images to be superimposed on a mathematical representation of the airplane to aid in interpreting the data. The procedures used for the graphic analysis technique used are described in previous reports¹⁰⁻¹¹. Brief further discussion of the techniques developed during this experiment for quantifying in-flight flow visualization data, and some examples of data for a baseline (no vortex flap) F-106B configuration are presented in the Appendix.

30° Vortex Flap

The primary characteristic of the flow field is the existence of a system of multiple vortices that appear to originate on the vortex flap and then migrate off the flap to run nearly streamwise over the wing as another vortex builds on the flap. This pattern is repeated many times down the wing, depending on angle of attack. It should be noted that smoke was only injected at one location (near forward part of segment 2a), and smoke was transported down the span after vortex migrations were seen to go over the wing. This indicates that there was some spanwise flow transport even when a new vortex appeared to be formed.

Figure 5 shows an example of a vapor screen image composite at an angle of attack of 9 degrees. Three distinct vortices are observed. At the most forward location, one vortex is forming on the flap surface, the second slightly inboard over the leading edge of the wing, and the third well inboard. The composite view of the vortices over the surface of the wing can be compared to the oil flow results shown in figure 6. The oil flow results confirmed the existence of a highly complex flow pattern with multiple vortex systems as observed during the vapor screen tests. It is seen that the primary flap vortex grows and the reattachment line reaches the wing leading edge midway in flap section 2a. This is indicated by the entrainment of oil that had flowed along the flap/wing leading edge juncture, which is then entrained in the vortex flow toward the flap leading edge. Looking further down the flap, the secondary separation line is clearly evident and at section 5b moves inboard off the flap to the wing. Under that peel-off, another vortex is formed which grows, and then peels off inboard at section 6b.

Effect of Angle of Attack

The primary characteristic of the flow field is the existence of a system of multiple vortices which appear to originate on the vortex flap and then migrate off the flap to run nearly streamwise over the wing as another vortex builds on the flap. This pattern is repeated many times down the wing, depending on angle of attack. The first shed vortex appears near 40° light sheet angle. A photograph taken during daylight with the smoke system running is shown in figure 7.

This picture shows at $\alpha=9^\circ$ the shedding process of the vortices leaving the flap surface and progressing over the wing surface. In this photograph, three vortices are seen to lift off the flap and go over the wing. The underlying surface flow corresponding to the shedding vortices is also evident from the flow cones attached to the flap. Due to the angle from which the photograph was taken, the cones that actually lie under the shedding vortices appear slightly outboard. As each vortex passes off the flap and onto the wing, the surface flow, as indicated by the cones, changes direction from nearly parallel to the wing leading edge to inboard along the path of the vortices.

Looking more closely, figure 8 shows a repeating pattern down the flap at sections 2a, 2b, 3a, 4, and 5a. The pattern is evidenced by the distortion of the normal herringbone pattern characteristic of a vortex scrubbing on a surface. These distortions probably indicate the influence of a peeling vortex and the growth of a new vortex underneath. Section 3a shows a clear discontinuity in the secondary separation line as does section 5b and 6b clearly indicating the formation of a new vortex. The oil flow data also showed that in general, the vortex reattachment line was near the wing/flap attachment line, which was the design philosophy for the flap. Figure 9 shows an approximation of the vortex paths over the wing based on the centroid of the smoke flow seen from both side and top camera views. The process used to determine the vortex paths from the vapor screen images is discussed in the appendix. It is important to note that the positions of the vortex over the flap include only that portion of the vortex visible in the light sheet, and in reality, if the complete vortex could be seen, it would probably show the vortex more outboard over the surface of the flap. Four vortex paths were seen. The furthest inboard vortex was seen only at one light sheet station (depicted as one symbol) just inboard of the wing leading edge. Two downstream vortices are seen to co-exist on the flap for a short distance before streaming aft over the wing. Finally, a fourth vortex path is observed on the flap surface outboard. At $\alpha=9^\circ$, no further vortices are seen aft on the wing, probably due to the small relative size of the vortices, and smoke entrainment and volume of smoke issues, however, as previously noted, the surface oil flow data show continued vortex activity down the length of the flap. The agreement between the observed surface flow information and off-surface core location is very good. Additionally, the surface flow data show the streamwise secondary separation lines originating each time near a discontinuity on the vortex flap surface - i.e. at a flap joint. Based on the surface flows, the vortex shedding process occurred several more times outboard on the flap.

Figure 10 shows the composite result of the vapor screen data at $\alpha=11^\circ$. Here, the top portions of some of the vortices are seen above the flap surface, in addition to the shed vortices over the wing surface. The data show good representation of 3 vortices trailing back nearly streamwise over the wing surface. The growth of the vortices on the flap before turning streamwise is also shown. The vortices on the flap surface are larger than was seen at $\alpha=9^\circ$ at each lightsheet location. Again, as was seen at $\alpha=9^\circ$, the smoke/light combination did not allow visualization of the vortex system on the outboard portions of the wing, or on the flap surface.

A sketch of the vortex paths at $\alpha=11^\circ$ is shown in figure 11. Three vortex paths are observed in the data, similar to the $\alpha=9^\circ$ case, however vortex paths are visible further down the length of the flap. The spanwise positions of the vortices and the locations at which the vortices cross over from the wing to the flap are slightly inboard compared to the $\alpha=9^\circ$ condition.

Figure 12 shows the composite results of the vapor screen data at $\alpha=13^\circ$. At this angle of attack, the vortices have grown in size, and are visible higher above the flap surface than for the lower angles of attack. Again, similar characteristics, of the vortex growing on the flap and then shedding over the surface of the wing are seen. Figure 13 shows the corresponding surface oil flow patterns. At $\alpha=13^\circ$, the secondary separation line is further inboard from the flap surface compared to the lower angles of attack. Distortions in the oil flow patterns signal the shedding process, but are less apparent than for the lower angles of attack. At this angle of attack, the reattachment of the flap vortex is well up onto the wing by section 4. Also, the secondary separation line has moved well inboard of the leading edge of the flap. The changes in the location of the secondary separation line at the beginning of segment 2a, middle of segment 2b and

beginning of segment 3a are consistent with the multiple systems seen in the vapor screen images – though the movements of the secondary separation line are far less dramatic than seen in the previous conditions. Additionally, streaks on the wing surface track back to the discontinuities in the secondary separation line and also correlate with the positions of the systems seen in the vapor screen data. Figure 14 shows the apex area of the flap and wing in more detail. The primary flap vortex reattachment reaches the leading edge of the wing just prior to segment 2, and then moves onto the wing, indicating a higher angle of attack than design. Also, it is interesting to note that the flow outboard of the secondary separation line is parallel to the leading edge of the flap.

The vortex path locations, shown in figure 15 are very similar to those seen at $\alpha=11^\circ$. Again, 3 vortices are evident originating from the flap, proceeding a short distance down the flap and then turning streamwise over the wing surface. The location of the separation lines in the oil flow results and the core paths show excellent agreement again. At this angle of attack, streamwise secondary separation lines were not evident on the flap, however bending of the secondary separation line after the flap joints beginning segments 2b and 3a indicate a flow protuberance probably associated with the streamwise vortex phenomenon. This weak interaction on the surface flow indicate that at high angles of attack, the streamwise vortices consist of a portion of the leading edge vorticity which becomes lifted significantly off the surface of the flap before streaming aft. The third vortex remains on the flap surface until disappearing from view due to the insufficient contrast. The oil flow results were inconclusive in determining if additional streaming vortices existed over the wing.

Figure 16 shows the composite result of the vapor screen data at $\alpha=15^\circ$. At this angle of attack, the flow condition is similar to that at $\alpha=13^\circ$, but the vortices have grown in size. Again, the flow is comprised of 2 vortices over the forward portion of the wing. Outboard, the vortex over the vortex flap grows and moves inboard. Concurrent with the inboard shift of the most outboard vortex, the inboard vortex disappears, which may indicate that the 2 vortex systems have merged. At the far outboard portion of the wing, the vortex is barely visible, probably because the larger vortex system inboard diffused the seeding smoke such that little smoke density was left at the aft or outboard locations.

The vortex path locations are shown in figure 17. An interesting feature of the flow is that increasing angle of attack does not significantly affect the span-wise location of the vortices as they trail over the wing. At each angle of attack, 3 vortices were seen over the flap and wing (one additional vortex was seen at the point nearest the apex at $\alpha=9^\circ$). The spanwise locations of the vortices near their originations are nearly identical to the $\alpha=13^\circ$ case. Progressing aft, the most inboard vortex appears to be merging with the adjacent vortex. Further aft, the combination of the two most inboard vortices may merge with outboard vortex, although the inflight images were inconclusive. The outboard vortex is much larger than it was at $\alpha=13^\circ$, and moves inboard over the wing surface.

Effect of Sideslip

The effect of sideslip was to effectively reduce or increase the sweep angle of the wing. Because the vortex flaps were designed specifically for 60° sweep angle, the performance of the flap would be expected to decrease as sweep angle was varied. Comparisons of the effect of sideslip will be made by individual light sheet location data. Only two sets of data were available at comparable angles of attack and sideslip for analysis from the flight program. These were at $\alpha=11^\circ$, and one point at $\beta=7^\circ$ at a lightsheet angle of 88° , and one condition at $\beta=-7^\circ$ at a lightsheet angle of 58° . Figure 18 shows the effect of negative sideslip at $\alpha=11^\circ$, and a lightsheet angle of 58° (near the forward section of the wing and flap). These data were recorded on the wing apex camera. At negative sideslip, the data show 3 distinct vortices compared with the larger, less defined structure at $\beta=0^\circ$. At $\beta=0^\circ$, the leading-edge vortices have started merging together on the surface of the wing at this lightsheet position. At $\beta=-7^\circ$, they have not yet coalesced, so the structure corresponds to a lower effective angle of attack condition.

A positive sideslip condition comparison is shown in figure 19. These data were recorded on the top view camera. Comparing the images at a lightsheet location of 88° and $\alpha=11^\circ$ for $\beta=7^\circ$ with corresponding $\beta=0^\circ$ data shows that the positive sideslip resulted in a larger flap vortex which corresponds to an increase in effective angle of attack. At sideslip, not only is the vortex on the surface of the flap (furthest right in the figure) larger than at zero sideslip, but the track of the shed vortex on the wing (second from right) is closer to the flap as well. The inboard vortex shed over the surface of the wing seen at zero sideslip is not well defined at the positive sideslip condition.

40° Vortex Flap

Effect of Angle of Attack

Similar flow patterns were observed for the 40° flap deflection angle as were previously seen for the 30° deflection, however the larger deflection angle tended to increase the angle of attack for similar flow conditions, and many more distinct vortices were visible as the light sheet swept aft.

Figure 20 shows an example of a composite view of the vapor screen data at $\alpha=11^\circ$. The 40° vortex flap proved even more susceptible to the multiple vortex system/vortex shedding phenomena than the 30° flap. Figure 21 shows the oil pattern at $\alpha=10^\circ$ showing the discontinuity of the secondary separation line and the path of the shedding vortex over the flap onto the wing occurring at every flap joint. It is postulated that the small geometric discontinuity between flap segments was a trigger to initiate the vortex shedding. The joints between segments were taped on some flights to prevent the possibility of air from spilling between segments, however no difference in the oil flow or smoke patterns were noted. In addition to the shedding vortex paths at most of the flap joints, this figure also indicates an apparent shed vortex approximately two-thirds back on segment 1 (light oil streak line running from secondary separation line near flap leading-edge and going up over the wing in a nearly streamwise direction), where there is no obvious geometric discontinuity.

At $\alpha=11^\circ$ (figures 22 and 23), the oil flow results are very similar to $\alpha=10^\circ$, except the streamwise streak lines on segments 3a and 4 are much more diffuse, indicating a different flow pattern developing as the angle of attack is increased. Figure 22 shows the forward portion of the flap at $\alpha=11^\circ$. The photograph shows that the flap vortex reattachment line is generally on the flap surface. Streamwise streak lines indicating shed vorticity are seen emanating from the leading edge of each flap segment starting with 2a. Discontinuities in the secondary separation line are visible in sections 2b and 3b. Figure 23 shows the aft half of the flap at 11° . Indications of shed vortices are again seen in each segment of the flap. Segment 5b shows a large discontinuity in the secondary separation line. The vortex-shedding pattern continues through the last flap segment. It should be noted that although clearly multiple vortices are being shed over the sing surface from the vortex flaps, the existence of a spanwise flow transport mechanism still existed (since smoke could be seen at outboard wing and flap locations).

Figure 24 shows the composite view of the vapor screen results at $\alpha=13^\circ$. The smoke flow indicate very similar patterns, with the multiple vortices shed off the flap and over the wing, as seen in the $\alpha=11^\circ$ data. The vortex size is increasing with the increase of angle of attack, and now the top of one of the vortices on the vortex flap can be seen at a lightsheet angle of 88° .

Figure 25 shows the oil flow pattern at $\alpha=13^\circ$. The primary reattachment line is very near the flap/wing junction indicating that the flow on the flap is at near design conditions. Again, discontinuities are seen in the secondary separation line, which has become very wide, and possibly a pooling of oil from more than one vortex, at every flap segment. The distortion of the herringbone patterns on the flap surface is evident in segments 2b, 3b, 5a, 5b, 6a and 6b. The absence of distortions in the herringbone pattern on some of the segments, especially segment 3a is puzzling since the vapor screen images showed vortex systems which would be emanating from this area, and a trace of oil is seen on the wing inboard of this flap segment. The secondary attachment line in segment 3a shows part of it starting from 0% chord at the leading edge of segment 3a.

Figure 26 shows the composite view of the vapor screen images at $\alpha=15^\circ$. At this angle of attack, the vortex size has increased again, and up to seven vortices can be seen on the aft portion of the wing. The larger deflection of the vortex flap, in addition to possible small vortex size on the flap before shedding, results in no vortices being seen in the lightsheet flow visualization over the inboard segments of the flap.

The oil flow data (figure 27) indicate the primary reattachment line was well up onto the wing. The secondary separation line shows discontinuities in its path which are evident near each flap segment joint through segment 3b. Figure 28 shows a closer view of the forward half of the flap. A sharp discontinuity in the secondary separation line is evident at segment 2a. The herringbone pattern distortion is evident only in section 3b, however the streaks over the wing indicative of a

vortex path seen in this figure and previously in figure 27 correlate well with the observed vapor screen data. The changes in path direction of the secondary separation line (near the flap leading edge) have indicated changes in the vortex structure. This, along with the oil streaks seen on the wing surface, indicate that some shedding of the vortex flow is occurring, although perhaps not as strongly as seen at the lower angles of attack. Possibly, the vortex systems are beginning to merge into fewer discrete shedding vortices at this point.

The composite view of the vapor screen data corresponding to $\alpha=18^\circ$ is shown in figure 29. At this angle of attack, the vortex systems have merged on top of the wing into two large vortices.

Effect of Mach Number

It is well known that Mach number can play an important role in vortical flowfield strength. Data were obtained at transonic conditions to attempt to visualize flowfield differences. At the higher Mach numbers, due to colder temperatures resulting from higher altitudes required, and due to higher airspeeds, less smoke was available to entrain in the vortex system. As Mach number was increased to from 0.80 to 0.90 at a constant angle of attack of 11° , the vortices observed on the wing appeared to lift slightly higher off the wing surface, and grow slightly in size. Due to the conditions mentioned, and the few test points that were flown, detailed data were not obtained to accurately assess the effects of Mach on effects of the vortex formation across angle of attack, or details above the surface of the vortex flaps.

Effect of Reynolds Number

Previous work conducted on the baseline F-106 (without the vortex flaps) showed a dominant effect of Reynolds number on the formation, growth and character of the vortex system over the wing⁶. Those results showed that at low Reynolds numbers, vortex formation began at lower angle of attack than at high Reynolds numbers. Additionally, the unmodified wing developed a multiple vortex system similar to that seen with the vortex flaps, however at the lower Reynolds numbers, fewer individual streaming vortices were formed. The location of the vortices at low Reynolds numbers was found to be inboard of the corresponding vortices at higher Reynolds numbers.

With the vortex flap, aerodynamic characteristics over the wing were found to be qualitatively invariant with Reynolds number over the range for which the flights were flown. The high altitude data shows less contrast than the low altitude data due to the decreased performance of the propylene glycol system at reduced atmospheric pressures and temperatures, however the overall flowfield characteristics remain unchanged. Planform views of the vortex positions over the wing are shown in figures 30 - 32 comparing the high and low Reynolds number data. Figure 30 shows the vortex positions at $\alpha=13^\circ$. Comparison of the data at 46 and 33 million Reynolds number shows nearly identical vortex placement on the surface of the wing. At $\alpha=15^\circ$, (figure 31), the 42 million Reynolds number data shows the vortex positions to be slightly inboard of the vortex positions at 29 million Reynolds number. Both sets of data still exhibit the same number of shedding vortices, (7), and they follow similar paths down the wing. At high angles of attack, (figure 32), the 27 million Reynolds number data at $\alpha=17^\circ$ maintains 3 separate vortices over the wing, whereas the 37 million Reynolds number data at $\alpha=18^\circ$ shows only 2. This may be an indication of flow sensitivity to angle of attack rather than Reynolds number.

Flight Data Discussion

Analysis of the surface flow visualization results showed two primary flow patterns. These are illustrated in figure 33. Both patterns show an apparent pooling of the oil along a line oriented in a nearly streamwise direction on the flap, and both patterns exhibit turning of the flow (streak lines) from an outboard orientation (characteristic of lying beneath a vortex) to an orientation nearly parallel to the flap hinge inboard of the disturbance line. The type-1 pattern (an example in fig 8, segment 5b) shows the streak lines continue to turn toward a streamwise direction as they near the disturbance line. This is consistent with the disturbance line indicating the secondary separation of a vortex path that has left the flap surface, and is shedding streamwise over the wing. Outboard of this streamwise pool of oil (disturbance line) is a region of strong shear flow where little or no detail can be seen in the oil flow data. After the disturbance, the secondary separation line outboard of the disturbance is repositioned very close to the flap leading edge indicating that the vortex outboard of the disturbance seems to have started from zero size. However, as previously mentioned, since smoke flow details were observed aft of these disturbances, some flow mechanism existed to enable spanwise flow across the areas of vortex shedding.

The type-2 pattern (an example in fig 6, segment 2b), generally has a less pronounced disturbance flowing streamwise, and the streak lines under the leading-edge vortex turn sharply back toward the leading edge before resuming the normal vortical flow pattern. This flow results in the appearance of a slight pooling of oil along the streamwise disturbance line, but there appears to be no net surface flow in the streamwise direction along that line except in the vicinity of flow reattachment where the streak lines from inboard continue to turn toward a streamwise direction and flow aft onto the wing. The secondary separation line aft of the disturbance does not reposition as close to the flap leading edge as seen with the type-1 pattern. It is not clear if this type-2 flow resulted in the development of a new leading-edge vortex system, or in a modification of the vortex system that existed further inboard on the wing.

Analysis of the data showed that in general, for low angles of attack, the type-1 vortex pattern dominated the flowfield characteristics. As angle of attack was increased, and the leading-edge vortex grew in size, the type-1 pattern transitioned to the type-2 pattern. As angle of attack was further increased, the type-2 pattern became less pronounced, and the flow began to be dominated by one or two leading-edge vortices. Examinations of the flight results showed that the multiple streamwise vortices observed above the wing originated at the flap leading edge where individual flap segments were joined. Oil flow studies were conducted with the joints sealed with fabric-backed tape to prevent air leakage, and showed essentially the same results. These data indicate that the small geometric perturbations along the leading edge were sufficient to generate a leading-edge flow that was very complex and significantly different in details than that observed previously in wind tunnel model tests and in CFD calculations.

The major purpose for developing the vortex flap was to improve the lift-to-drag ratio at high maneuvering lift coefficients. Despite the strikingly different flow field developed on the airplane compared to CFD and wind tunnel predictions, the overall effectiveness of the flaps were very close to predictions. A comparison between flight and wind tunnel / simulation results of the maximum sustained load factor achievable at an altitude of 30,000 feet at maximum power is shown in figure 34. The data show that the vortex flap addition clearly improved transonic maneuvering capability, and the improvements were very close to predictions.

POST FLIGHT WIND TUNNEL INVESTIGATION

After observing the unpredicted vortex topologies in flight, an F-106 wind tunnel model was tested in the Langley 7-by-10 – Foot High-Speed Tunnel¹². Flow visualization tests were conducted using a surface oil flow test technique at low subsonic speeds. All previous wind tunnel tests had shown a single leading-edge vortex system along the flap, as predicted by the design methodology. During storage of the model, some minor damage in the form of small dents and nicks had occurred to the flaps. Since leading-edge discontinuities were believed to be at least partially responsible for the multiple vortices seen in flight, these dents were not repaired prior to the tests. It was found during the test that the dents, or the subsequent application of tape flow trips, would provide sufficient perturbation for the shedding of vortices and formation of the multiple vortex system seen in flight. The extremely small perturbation size indicated that with normal manufacturing tolerances, it might be impossible to avoid the multiple vortex patterns seen in flight on a full-scale airplane with leading-edge devices similar to vortex flaps. Examples of wind tunnel data results are shown in figures 35 and 36.

CONCLUDING REMARKS

Flow visualization studies were conducted on the F-106 vortex flap airplane to aid in the validation of vortex flap design tools. Surface flow visualization (oil and cones) and off-surface flow visualization (vapor screen) techniques were employed. Data were obtained at angles of attack from 7° to 18° and Mach numbers from low subsonic to 0.95.

The primary feature observed was the presence of multiple vortex systems over the flap. Both configurations tested showed similar qualitative results with vortices developing on the flap and then shedding over the wing. Small geometric discontinuities appeared to trigger the shed vorticity, however, the flap surface appeared to have a vortex along its span. The vapor screen data showed clearly the vortex on the flap growing with angle of attack and also as it moved downstream. Then, the flap vortex would shed off of the flap and progress nearly streamwise over the surface of the wing. Immediately under the shed flap vortex, a vortex began its growth on the flap surface and repeated this pattern of shedding many times down the length of the flap. Two flow field mechanisms appeared to exist on the flap surface. At

lower angles of attack, a very distinct vortex shedding and vortex formation pattern appeared several times down the span. At higher angles of attack, generally a less distinct surface flow pattern was observed, however the off-surface flow visualization indicated similar vortex flow shedding pattern over the wing. A span-wise flow transport mechanism existed across the span of the flaps, even with the shedding vortices, as evidenced by smoke entrainment visible over most of the span of the wing. Reynolds number effects, seen previously on the unmodified F-106 wing, were not evident with the sharp leading edge vortex flaps. Performance flight test results and subsequent wind tunnel studies showed that the effects of the unpredicted multiple vortex pattern appeared to be small, and confirmed hypothesis of small discontinuities being the trigger for the shed vortices.

Appendix on Flight Flow Visualization for Baseline F-106B Aircraft

Discussion:

The baseline aircraft, i.e. without vortex-flap, was tested at the end of the vortex-flap program using the same rotating vapor-screen technique – rotating light-sheet, on-board propylene-glycol-vapor-seeding-system and two video cameras – coupled with image enhancement, photogrammetry, and computer graphics. The purpose of the test was to provide understanding as to the origin of the multiple-primary vortices discovered during a prior test (ref. 6) of the baseline aircraft using a fixed light-sheet.

Sample false-color 2D results from reference 11 have been mapped onto the aircraft numerical-surface-geometry in 3D space as shown in figure A1. This figure demonstrates the utility of the rotating light sheet to provide global vortex information. From this figure, one can see evidence of a coherent vortex – the vortex core in each 2D image is essentially the brighter region – to form above this round-edged cambered-wing and to trail aft. Moreover, this vortex leaves its feeding sheet where a new and un-visualized off-surface vortex forms in the vicinity of the leading-edge slot – an aerodynamic fence.

Vortex properties of core and reattachment-point locations can be extracted from the 2D vapor-screen images of figure A1 by the methods outlined in figure A2. The core locations are determined by computer software which calculates a weighted average of the gray scale values of the reflected light in a user controlled, circumscribed region. The preceding was done because this cambered wing (with its round leading edge) tends to produce a diffuse vortex system, one in which the propylene-glycol condensed-particles do not revaporize in the core but merely concentrate (ref. 6). The determined location from this process is a centroid and is called the vortex core.

Using vapor-screen data to find an approximation of the reattachment point is not as straightforward, because, as shown in figure A2, the vapor particles provide only an envelope or filled outline of the vortex system. For results presented here, the core-locating software has been applied to determine the most inboard edge (inner extent) of the envelope. By projecting this portion of the vortex envelope to the wing upper surface, a track of the inboard extreme can be established. This surface location of the inner extent of the envelope can be used as an *approximation* of the reattachment point. The rationale for this statement is based on a study of figure A3 (See refs. 13 and 14). This led to a *hypothesis that the lateral difference between the projected vortex envelope and reattachment point is small*. Further discussions regarding this technique and potential sources of errors for determining the reattachment point using off-surface flow visualization data are included in reference 11.

Even with potential sources of error, this technique still provides a rational basis for estimating the reattachment location in those situations where surface techniques are not available. Comparisons with oil-flow results are presented in an attempt to gauge the reliability of this technique.

The resulting vortex-system core location(s) and reattachment point(s) for each image can be located (mapped) in 3D space through the process of photogrammetric reconstruction (See ref. 11). Hence, these results can be displayed as surface tracks mapped onto the wing planform; also, the distances to the local leading edge can be calculated along the light sheet for each rotation angle, Φ . Examples are given next.

Once vortex features can be quantified on the surface, other parametric studies can be done. For example, figure A4 shows the impact of altitude (Reynolds number - R_n) on **the distance along a light-sheet ray of the outermost vortex core to the local leading-edge (l)** for this aircraft at 1g, as determined from vapor-screen processing. The general trend of l is to be displaced inboard over the middle angle-of-attack (α) range

with increasing altitude. The altitude increase is associated with a reduction in R_n . Therefore, the inboard movement is reasonable because of flow separation and vortex merging occurring at the smaller α 's at the lower R_n 's. This effect of lower R_n results in the outermost vortex system tending to be a single vortex at a moderate α . Further, this system is likely to be larger and to have its core location more inboard. Conversely, for the higher R_n (occurring at the lower altitudes) a delay occurs in the separation process leading to vortex formation. Consequently, to maintain a fixed value of l as altitude decreases, α must increase. At $\Phi = 100^\circ$ there is an outward movement of the core at the lower values of α . For these maneuvers, R_n and α are inversely related and the l curves reflect this behavior.

These projected vortex-feature tracks can be compared with other data sources, such as oil-flow and pressure coefficient. Figure A5 shows a comparison with flight oil-flows. The dominant-vortex reattachment lines are in good agreement near Fuselage Station (FS) 490 and Butt Line (BL) 100, and the core track is well positioned with respect to the streak lines, although it is outboard of the closest secondary separation line. The surface streak lines do not indicate the presence of the inboard vortex determined from the images.

Figure A6 shows a similar comparison but here with the upper-surface pressure coefficient ($C_{p,u}$) data. This figure shows good correlation over the middle part of the wing between the core tracks and the pressure peaks, including the second peak of belt-set 3. [Note that in order to compare these two different kinds of results, the pressure-port locations associated with the peak surface pressures must be used.]

Concluding Remarks:

The conclusion from this appendix is that optical methods can be used in flight to provide aircraft flow features both on- and off- the surface and that they are worth the effort for increased flow understanding of other measured or predicted results.

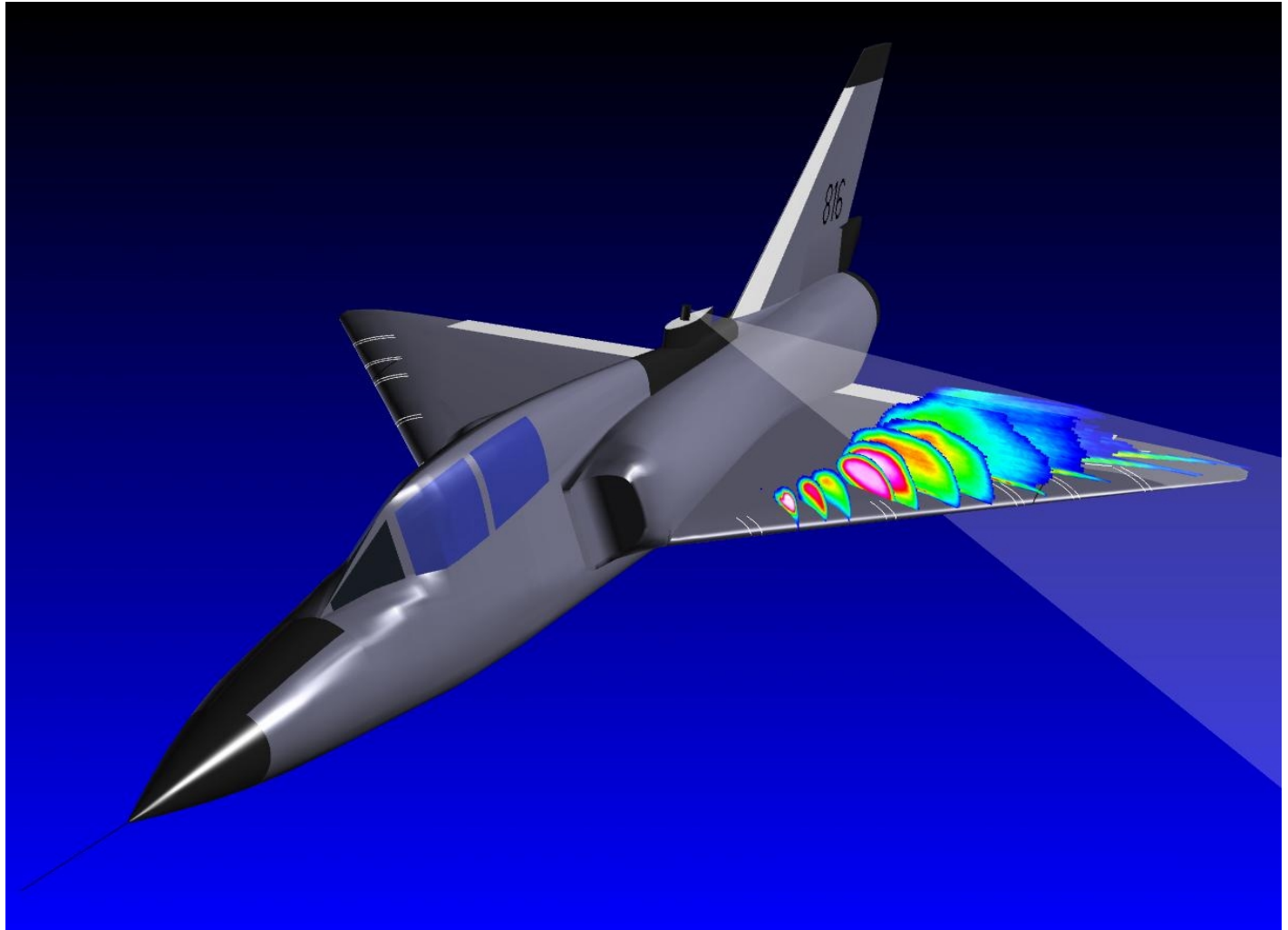


Figure A1. Three-dimensional representation of vortex-system images and characteristics on F-106B numerical surface geometry. (Note that paint lines occur on left wing but are displayed on right wing here, reflected about centerline, to show complete set of pertinent features represented in surface geometry.)

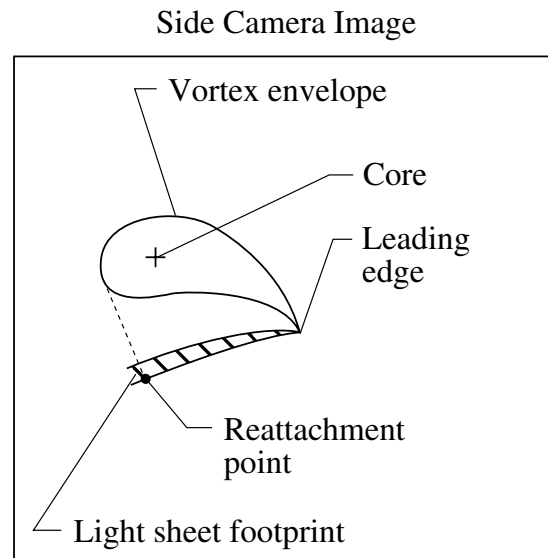
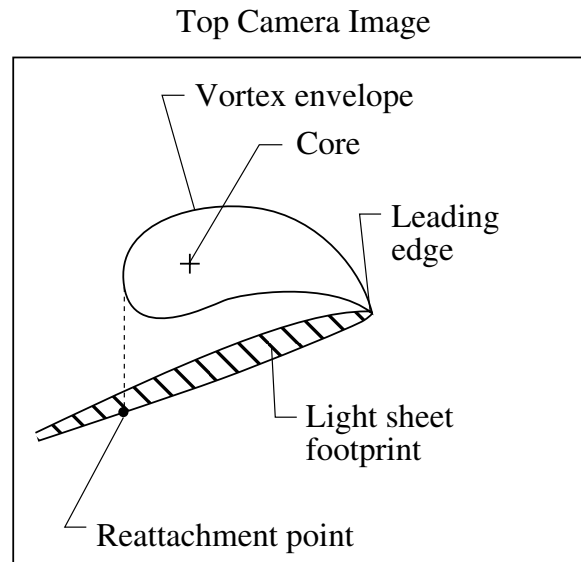


Figure A2. Illustration of reattachment-point location using a computer software (graphics) procedure.

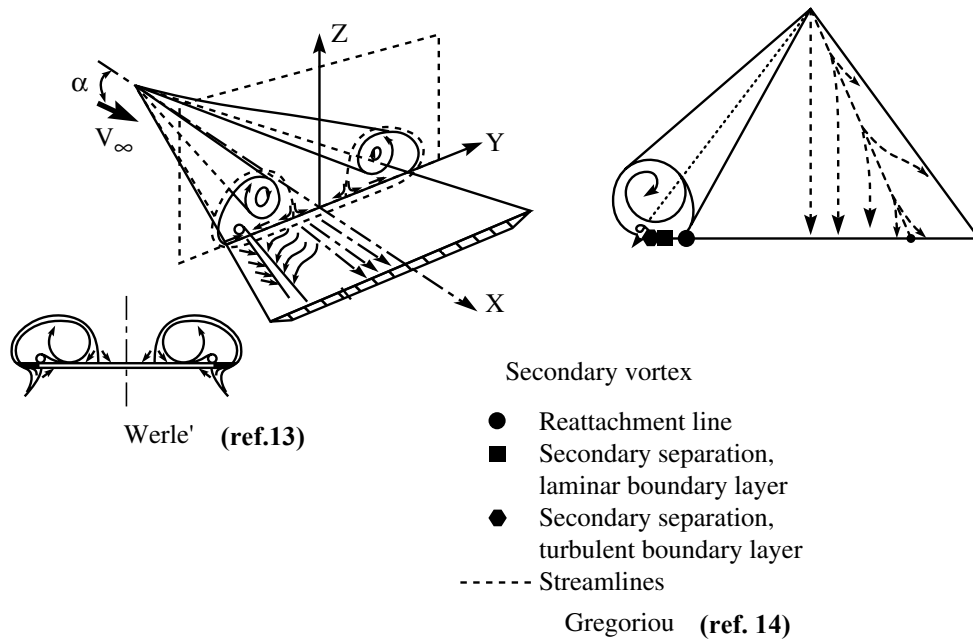


Figure A3. Representative sketches of off-surface vortex systems and associated surface flow.

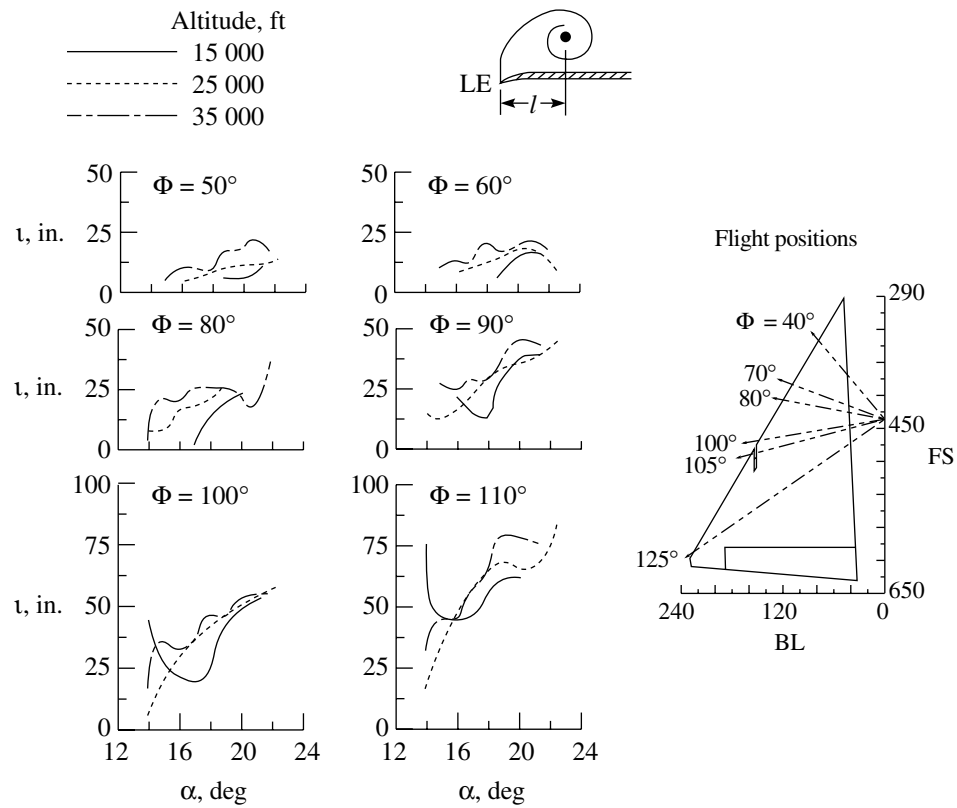


Figure A4. Effect of altitude (R_n) on distance from outermost (vapor-screen) to local leading-edge along light-sheet ray at 1g for F-106B aircraft.

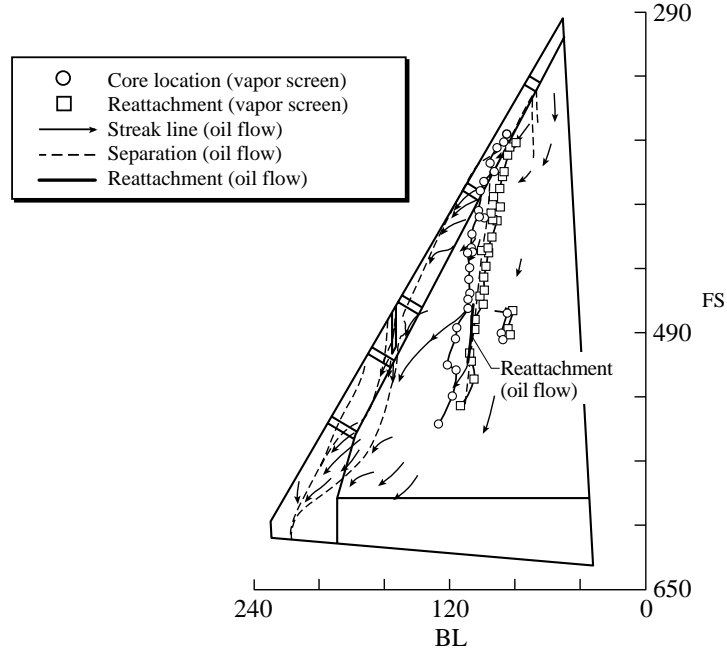


Figure A5. Superposition of projected vapor-screen results on oil-flow patterns with streak lines. F-106B; $\alpha = 18.6^\circ$; $M_\infty = 0.29$; $R_n = 30.0 \times 10^6$.

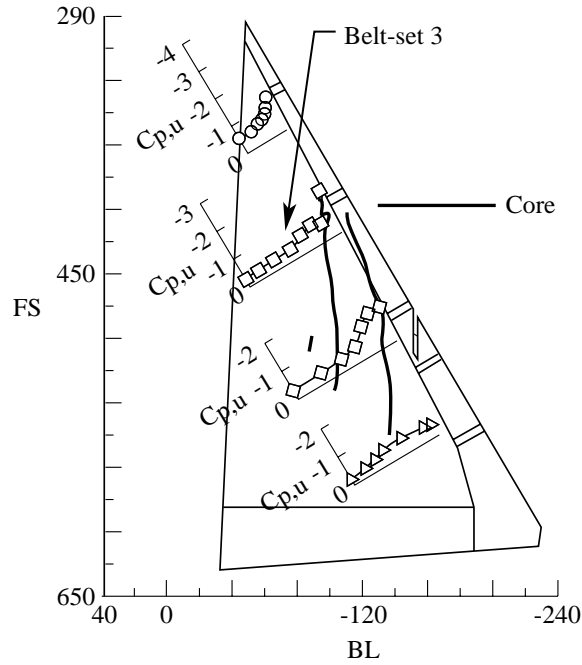
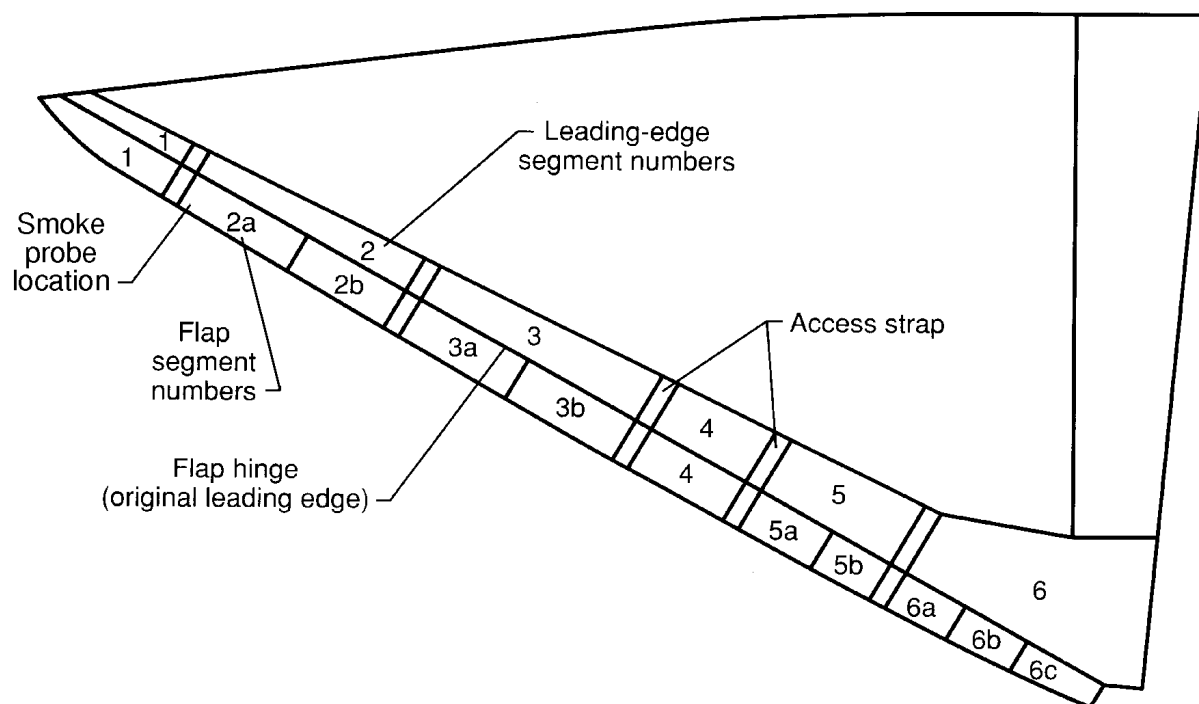


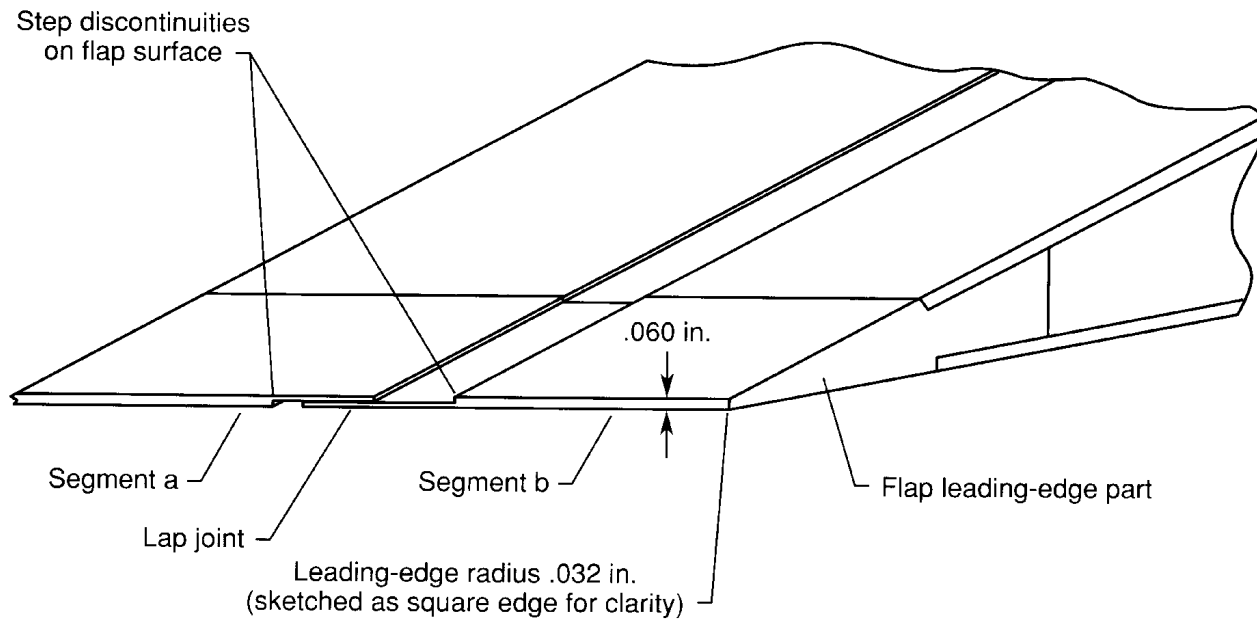
Figure A6. Superposition of projected vapor-screen core tracks on $C_{p,u}$. F-106B; $\alpha = 14.9^\circ$; $M_\infty = 0.41$; $R_n = 34.6 \times 10^6$.

REFERENCES

1. Rao, Dhanvada M.: Leading-Edge 'Vortex Flaps' for Enhanced Subsonic Aerodynamics of Slender Wings. ICAS-80-13.5, Oct. 1980.
2. Lamar, John E.; Campbell, James F.: Vortex Flaps – Advanced Control Devices for Supercruise Fighters. Aerospace America, vol. 22, no. 1, Jan. 1984, pp. 95-99.
3. Campbell, J.F.; and Osborn, R.F.: Leading-Edge Vortex Research: Some Nonplanar Concepts and Current Challenges. Vortex Flow Aerodynamics, Volume I, James F. Campbell, Russell F. Osborn, and Jerome T. Foughner, Jr., eds., NASA CP-2416, 1986, pp. 31-63.
4. Yip, Long P.; and Murri, Daniel G.: Effects of Vortex Flaps on the Low-Speed Aerodynamic Characteristics of an Arrow Wing. NASA TP-3106, 1991.
5. Frink, Neal T.: Refinements of a Vortex Flap Design Method With Systematic Applications. Vortex Flow Aerodynamics, Volume III, James F. Campbell, Russell F. Osborn, and Jerome T. Foughner, Jr., eds., NASA CP-2418, 1986, pp. 25.
6. Lamar, John E.; and Johnson, Thomas D.: Sensitivity of F-106B Leading-Edge-Vortex Images to Flight and Vapor-Screen Parameters. NASA TP-2818, June 1988.
7. Frink, N. T.; Huffman, J.K.; and Johnson, T.D., Jr.: Vortex flap flow reattachment line and subsonic longitudinal aerodynamic data on 50 deg to 74 deg Delta wings on common fuselage. NASA TM-84618, Dec. 1983.
8. Bare, E.A.; Reubush, D.E.; and Haddad, R.C.: Flow field over the wing of a delta-wing fighter model with vortex control devices at Mach 0.6 to 1.2. NASA TM-4296, April 1992.
9. Frink, N.T.: Subsonic wind-tunnel measurements of a slender wing-body configuration employing a vortex flap. NASA TM-89101, July 1987.
10. Stacy, Kathryn; Severnce, Kurt; and Childers, Brooks A.: Computer-Aided Light Sheet Flow Visualization Using Photogrammetry. NASA TP-3416, 1993.
11. Lamar, John E.; Brandon, Jay M.; Stacy, Kathryn; Johnson, Thomas D., Jr.; Severence, Kurt; and Childers, Brooks A.: Leading-Edge Vortex-System Details Obtained on F-106B Aircraft Using a Rotating Vapor Screen and Surface Techniques. NASA TP-3374, Nov. 1993.
12. Hallissy, James B.; Schoonover, W. Elliott, Jr.; Johnson, Thomas D., Jr.; and Brandon, Jay M.: Wind-Tunnel Investigation of the Multiple Vortex System Observed in Flight Tests of the F-106B Vortex Flap Configuration. NASA TP-3322, Dec. 1993.
13. Werlé, H.: Aperçu cu sur les Possibilités Expérimentales du Tunnel Hydrodynamique a Visualization de l'O.N.E.R.A. ONERA Tech. Note 48, 1958.
14. Gregoriou, Gregor: Modern Missile Design for High Angle-of-Attack. AGARD-LS-121/5, March 1982.



(a) Segmentation layout.



(b) Typical flap joint.

Figure 1. – Vortex flap construction details.

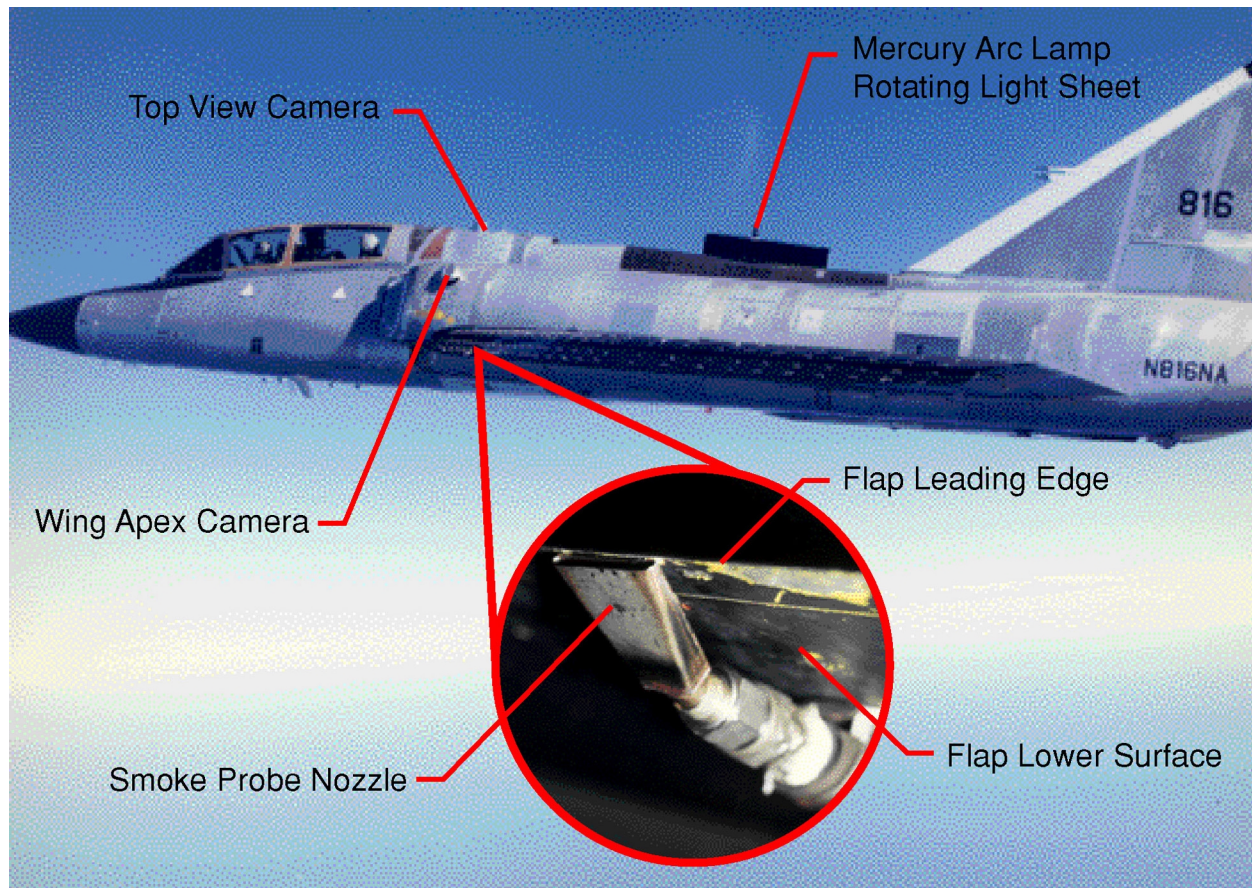


Figure 2. – Vapor screen flow visualization system.

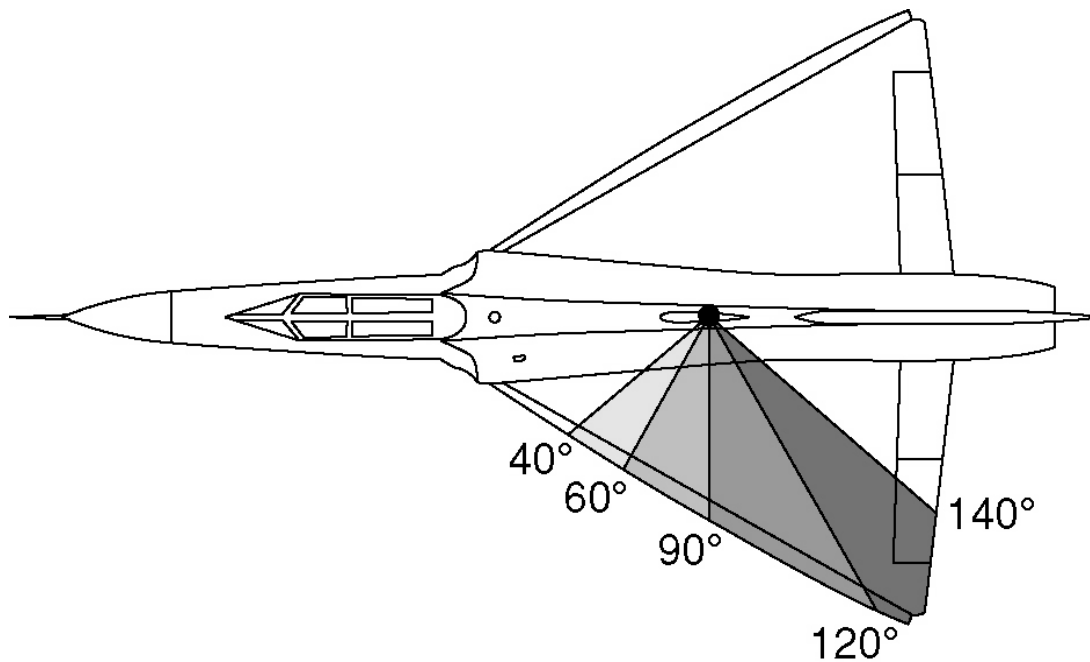


Figure 3. – Lightsheet azimuth coverage over the wing surface.

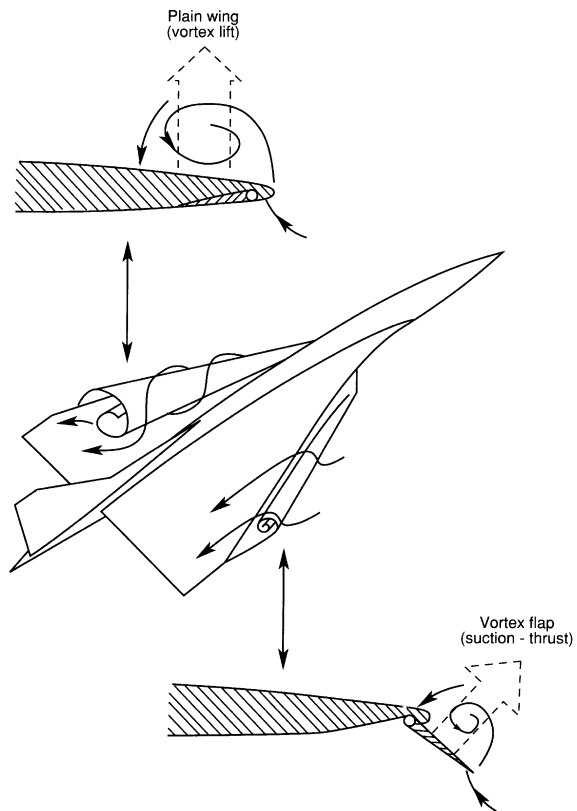


Figure 4. – Vortex flap concept.

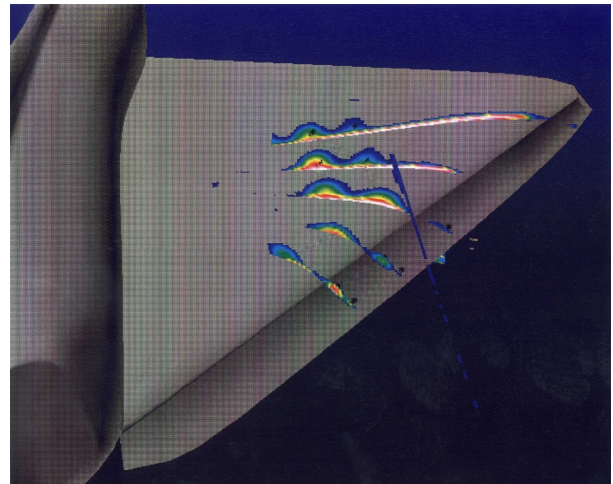


Figure 5. – Vapor screen image composite, $\alpha = 9^\circ, 30^\circ$ vortex flap.

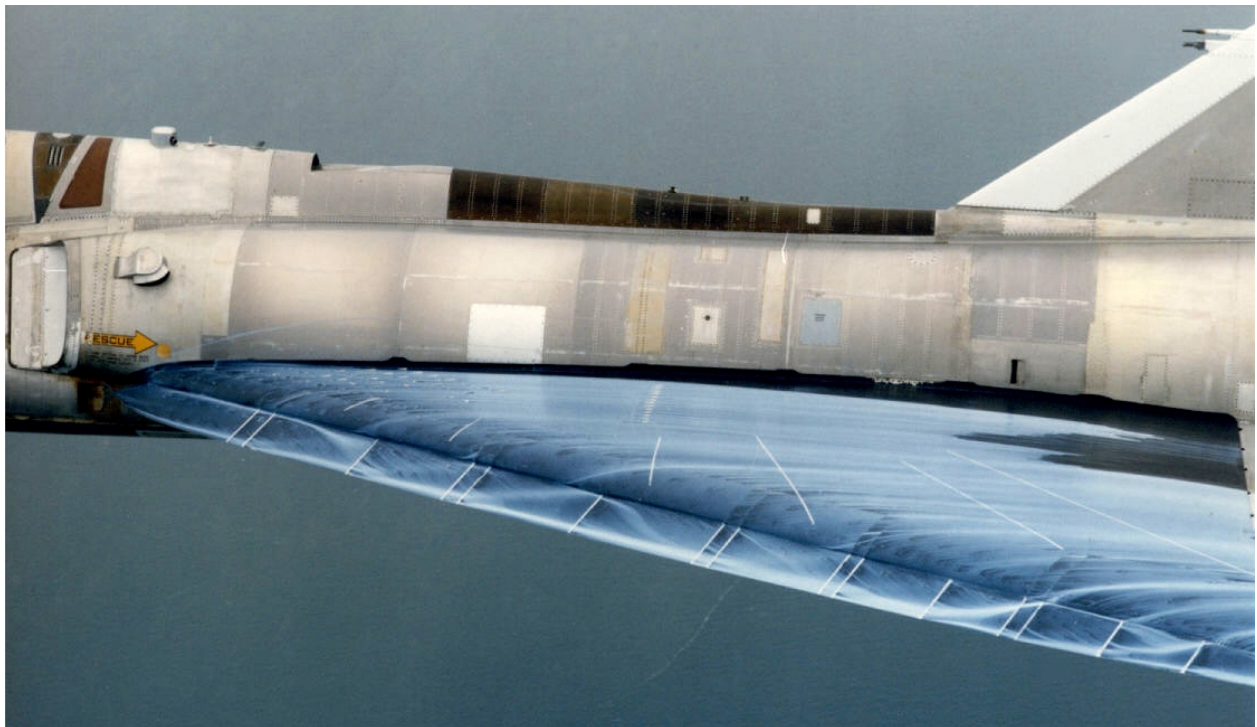


Figure 6. – Oil flow results at $\alpha = 9^\circ, 30^\circ$ vortex flap.



Figure 7. – Daytime smoke, $\alpha = 9^\circ$, 30° vortex flap.

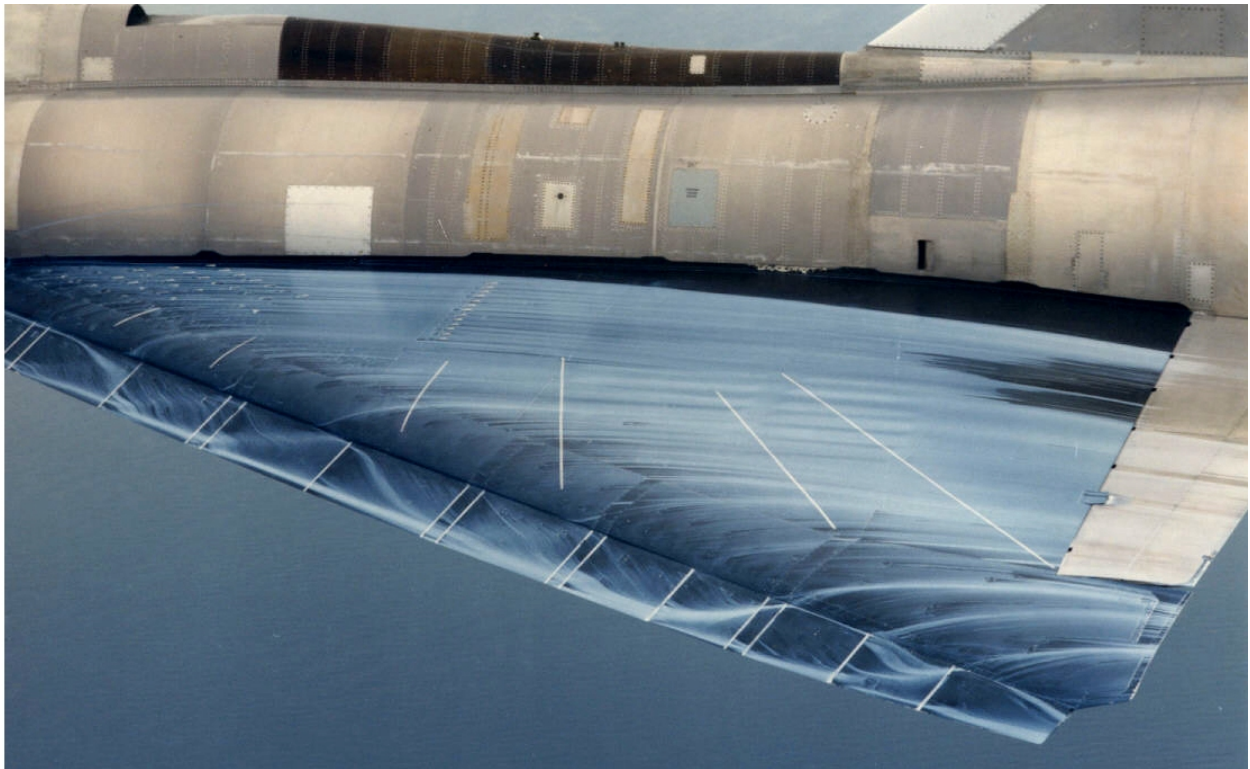


Figure 8. – Oil flow patterns, $\alpha = 9^\circ$, 30° vortex flap.

FLT 91-33/6, $\alpha = 9^\circ$, HP= 5,000', Mach = 0.37, $R_n = 53 \times 10^6$

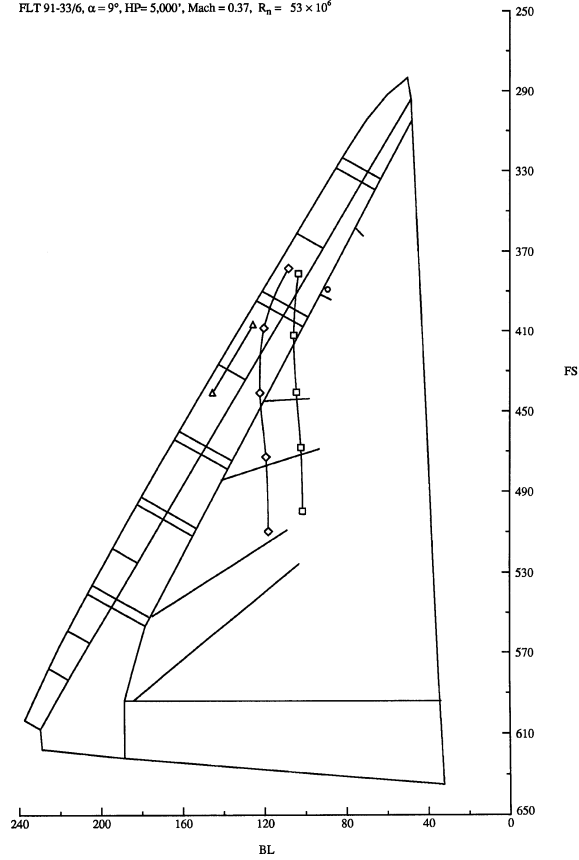


Figure 9. – Vortex paths, $\alpha = 9^\circ$, 30° vortex flap.

FLT 91-33/8 $\alpha = 11^\circ$, HP= 5,000', Mach = 0.32, $R_n = 46 \times 10^6$

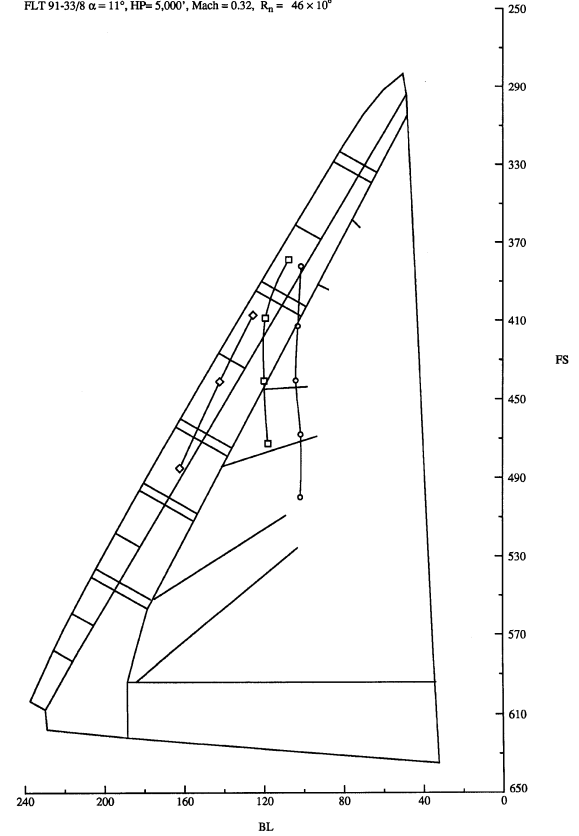


Figure 11. – Vortex paths, $\alpha = 11^\circ$, 30° vortex flap.

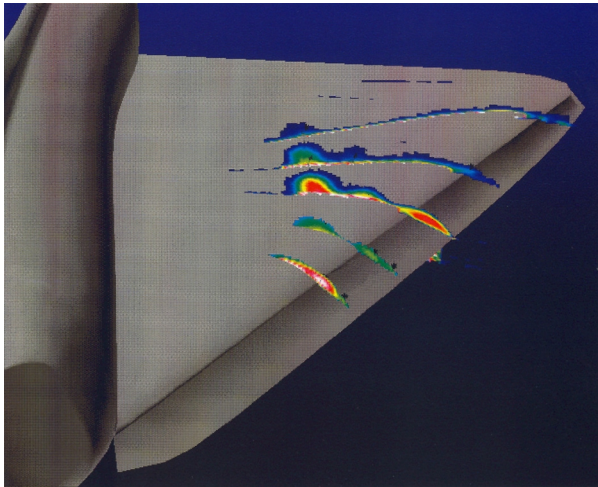


Figure 10. – Vapor screen composite, $\alpha = 11^\circ$, 30° vortex flap.

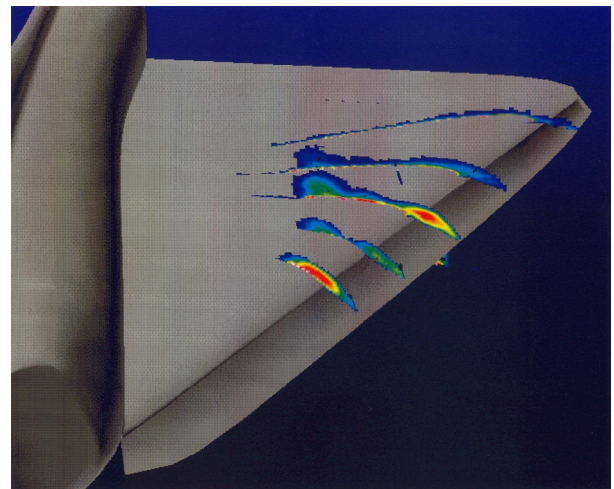


Figure 12. – Vapor screen composite, $\alpha = 13^\circ$, 30° vortex flap.



Figure 13. – Surface oil flow patterns, $\alpha = 13^\circ$, 30° vortex flap.

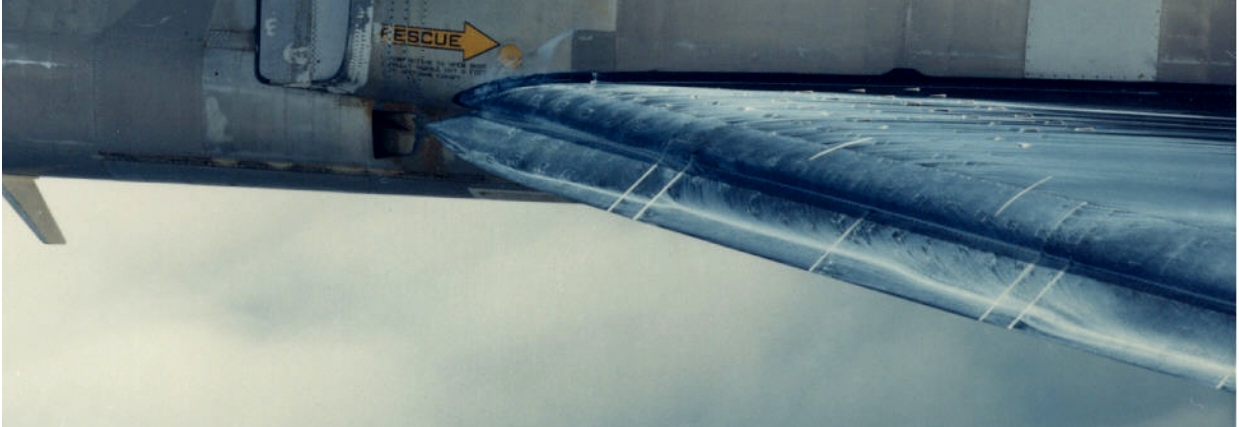


Figure 14. – Detail of apex area, $\alpha = 13^\circ$, 30° vortex flap.

FLT 91-33/10, $\alpha = 13^\circ$, HP= 5,000', Mach = 0.29, $R_n = 41 \times 10^6$

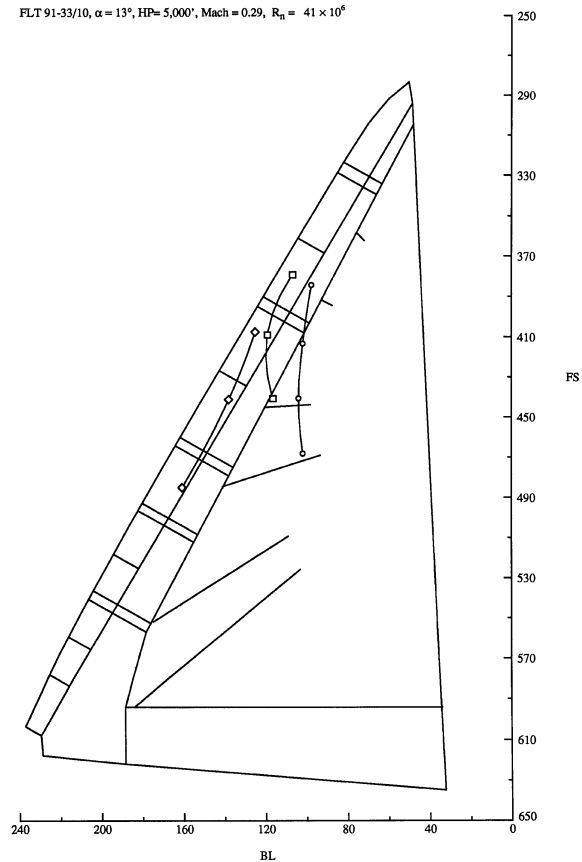


Figure 15. – Vortex paths, $\alpha = 13^\circ$, 30° vortex flaps.

FLT 91-33/12, $\alpha = 15^\circ$, HP= 5,000', Mach = 0.26, $R_n = 37 \times 10^6$

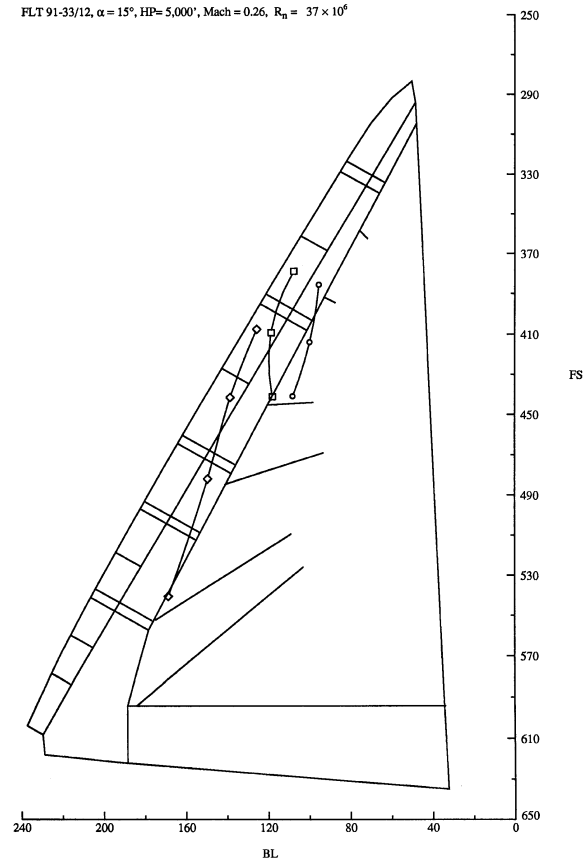


Figure 17. – Vortex paths, $\alpha = 15^\circ$, 30° vortex flaps.

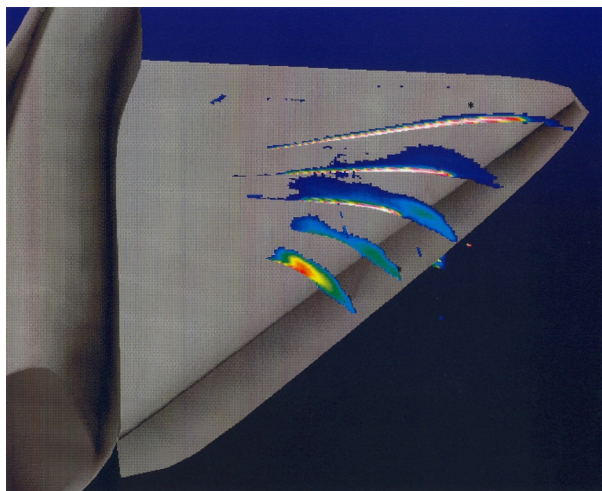


Figure 16. – Vapor screen composite $\alpha = 15^\circ$, 30° vortex flaps.

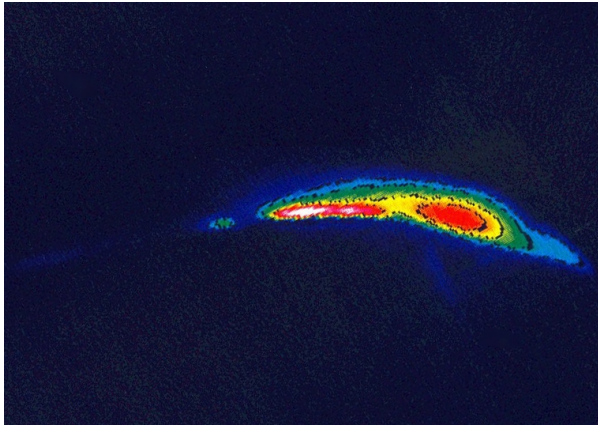


Figure 18(a). – View of vortex at lightsheet position of 58° , $\alpha = 11^\circ$, $\beta = 0^\circ$, 30° vortex flap.

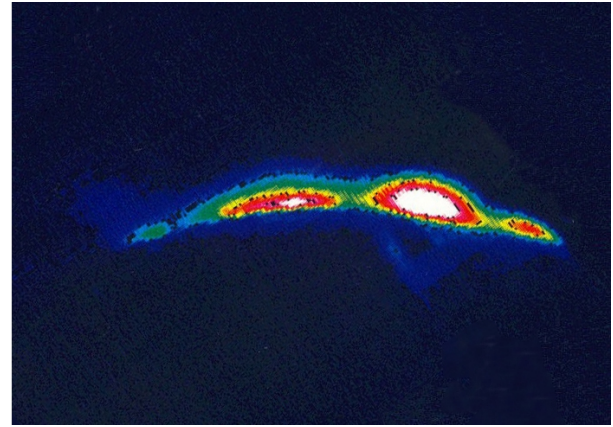


Figure 18(b). – View of vortex at lightsheet position of 58° , $\alpha = 11^\circ$, $\beta = -7^\circ$, 30° vortex flap.

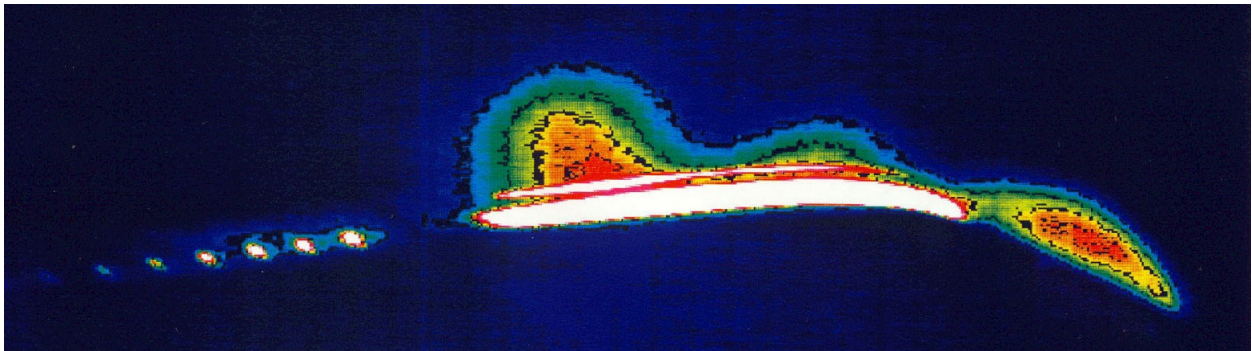


Figure 19(a). – View of vortex at lightsheet position of 88° , $\alpha = 11^\circ$, $\beta = 0^\circ$, 30° vortex flap.

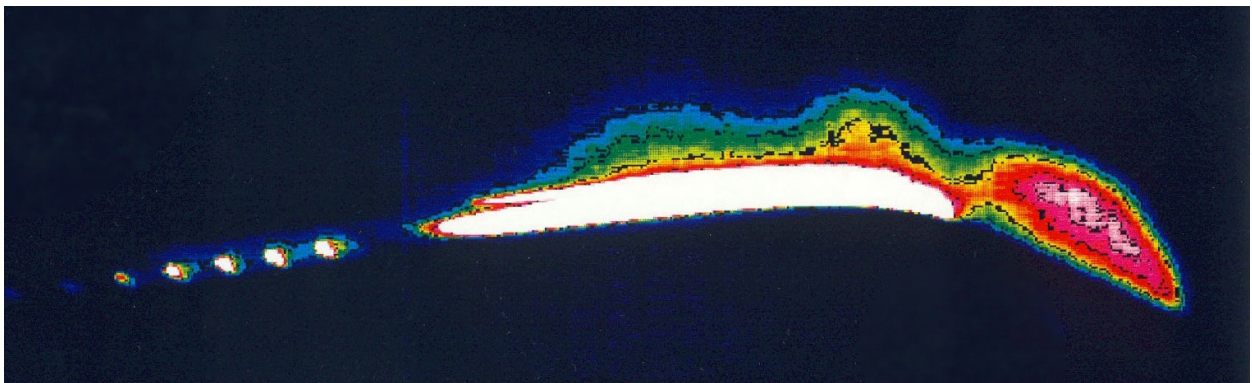


Figure 19(b). – View of vortex at lightsheet position of 88° , $\alpha = 11^\circ$, $\beta = +7^\circ$, 30° vortex flap.

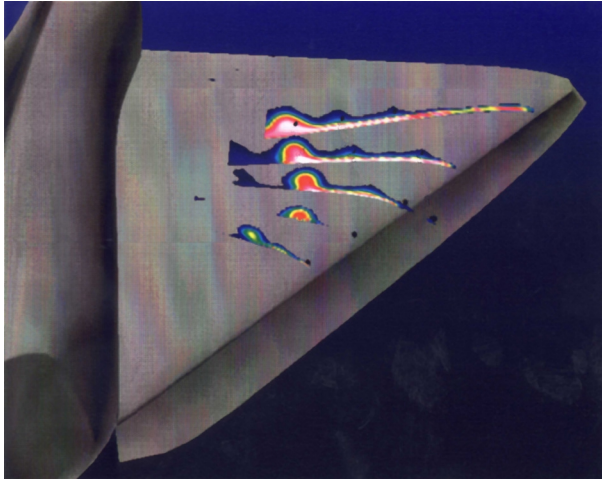


Figure 20. – Vapor screen composite, $\alpha = 11^\circ$, 40° vortex flaps.

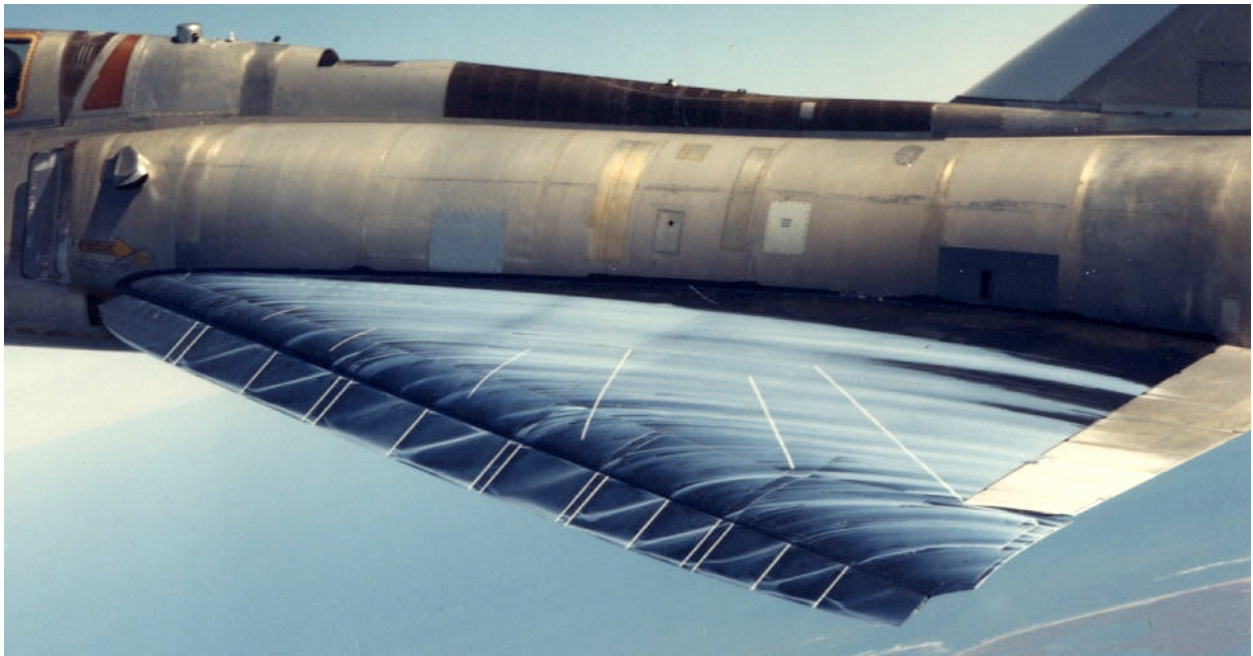


Figure 21. – Oil flow patterns, $\alpha = 10^\circ$, 40° vortex flaps.



Figure 22. – Oil flow patterns, $\alpha = 11^\circ$, 40° vortex flaps.

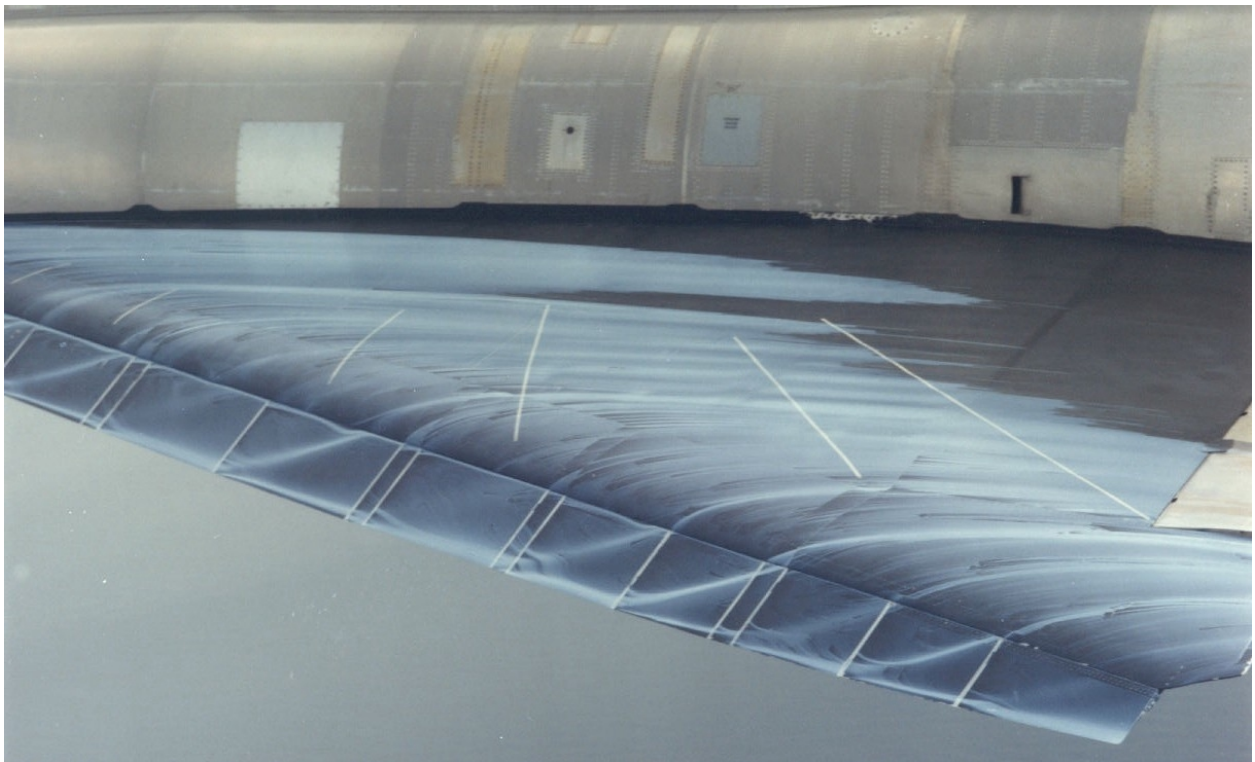


Figure 23. – Oil flow patterns on outboard segment of wing, $\alpha = 11^\circ$, 40° vortex flaps.

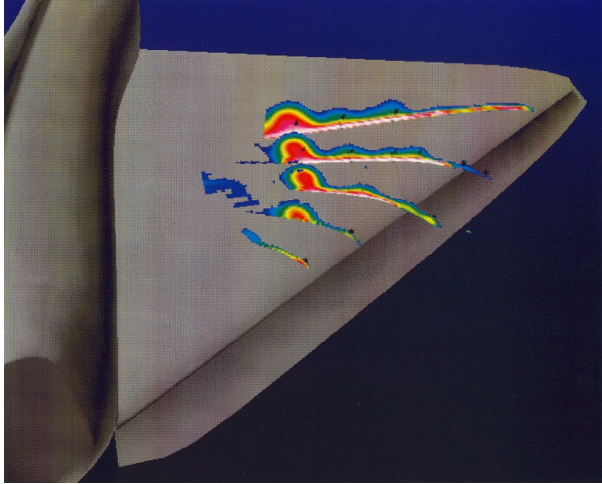


Figure 24. – Vapor screen composite, $\alpha = 13^\circ$, 40° vortex flaps.

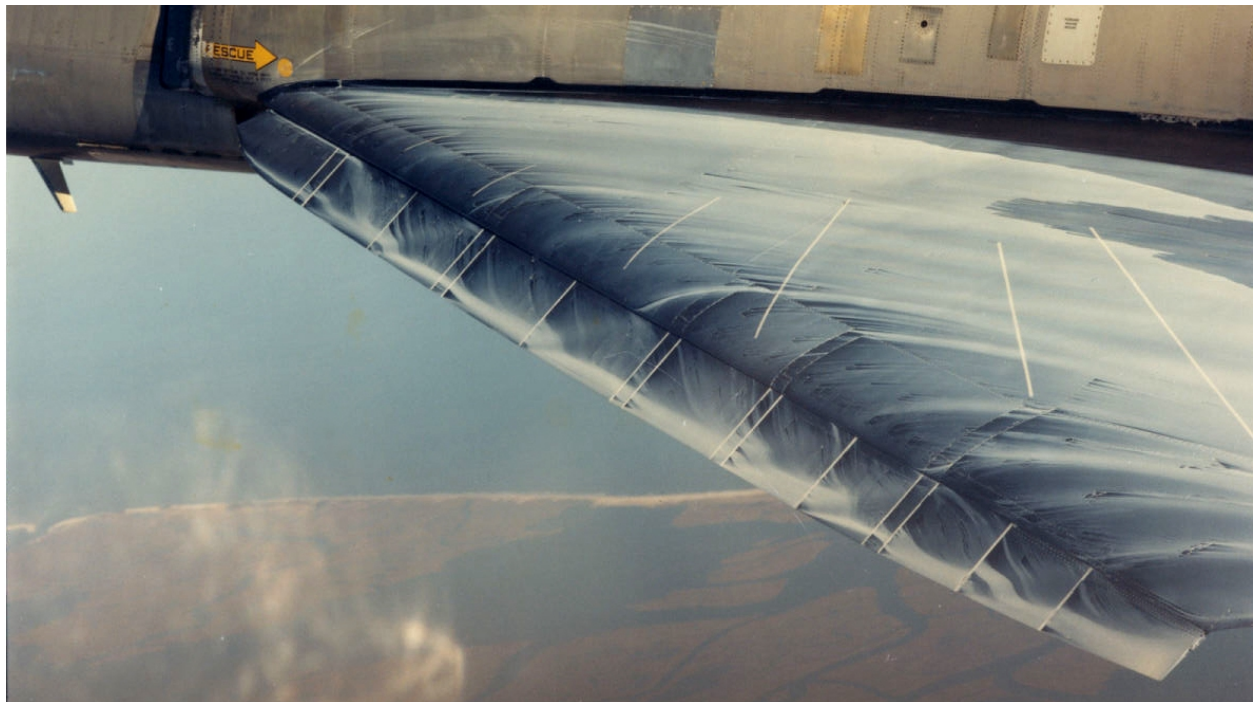


Figure 25. – Oil flow patterns, $\alpha = 13^\circ$, 40° vortex flaps.

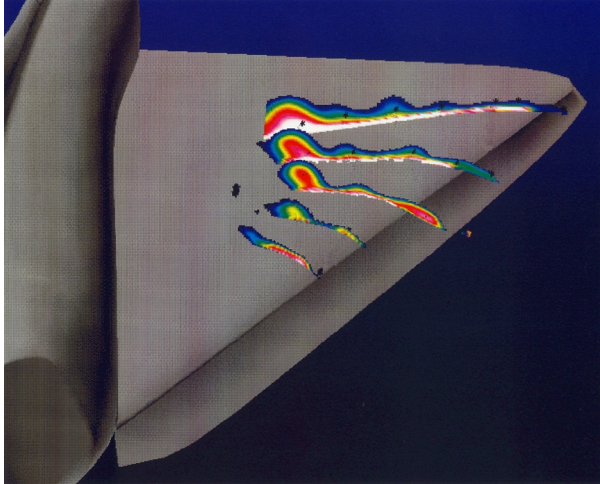


Figure 26. – Vapor screen composite, $\alpha = 15^\circ$, 40° vortex flaps.



Figure 27. – Oil flow patterns, $\alpha = 15^\circ$, 40° vortex flaps.



Figure 28. – Detail of forward sections of the vortex flap, $\alpha = 15^\circ$, 40° vortex flaps.

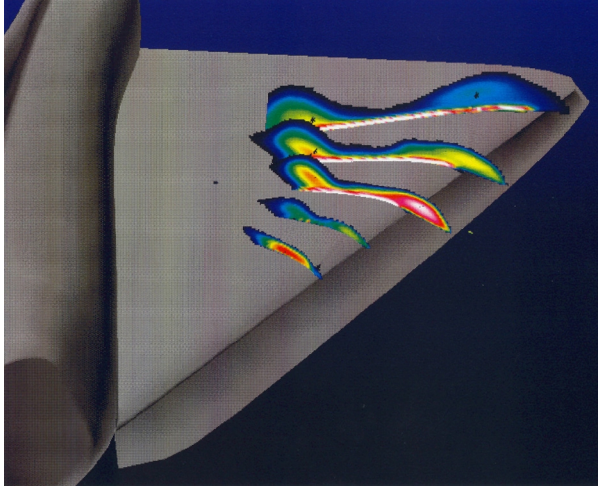


Figure 29. – Vapor screen composite, $\alpha = 18^\circ$, 40° vortex flaps.

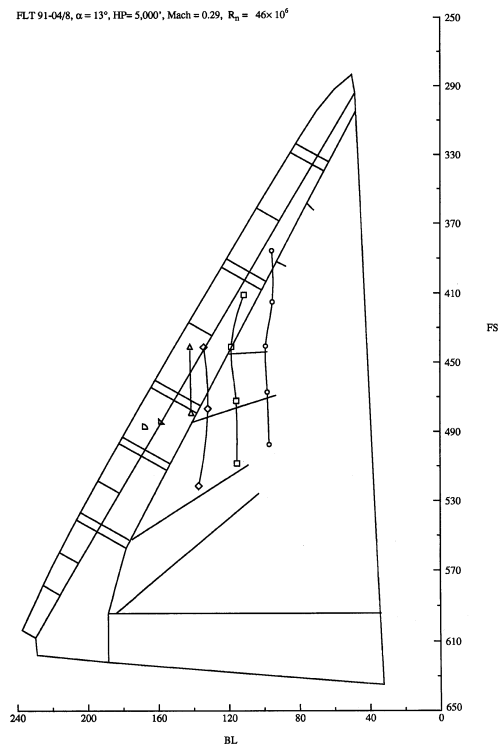


Figure 30(a). – Vortex paths, $\alpha = 13^\circ$, 40° vortex flaps, $Re = 46 \times 10^6$, Mach = 0.26.

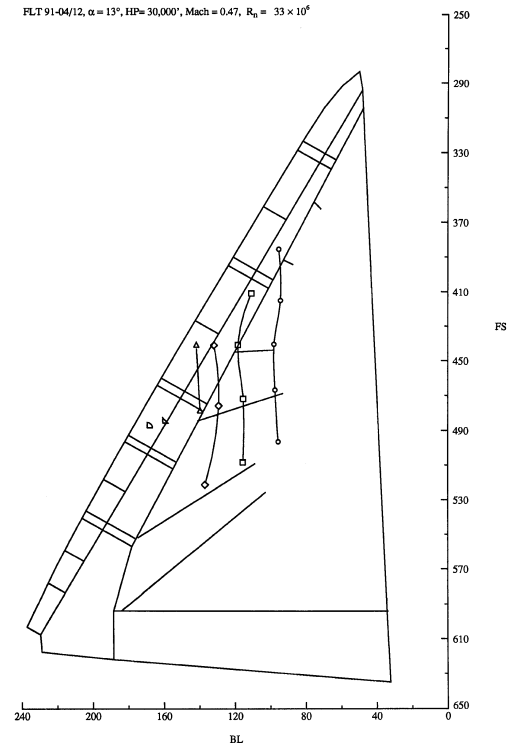


Figure 30(b) - Vortex paths, $\alpha = 13^\circ$, 40° vortex flaps, $Re = 33 \times 10^6$, Mach = 0.47.

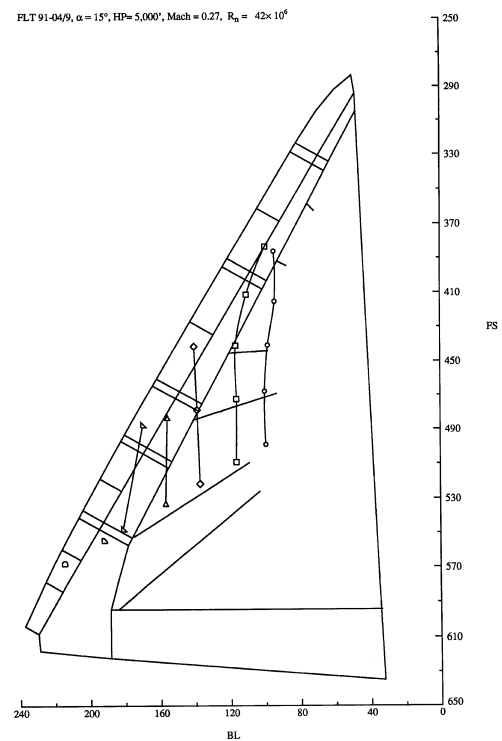


Figure 31(a) - Vortex paths, $\alpha = 15^\circ$, 40° vortex flaps, $Re = 42 \times 10^6$, Mach = 0.27.

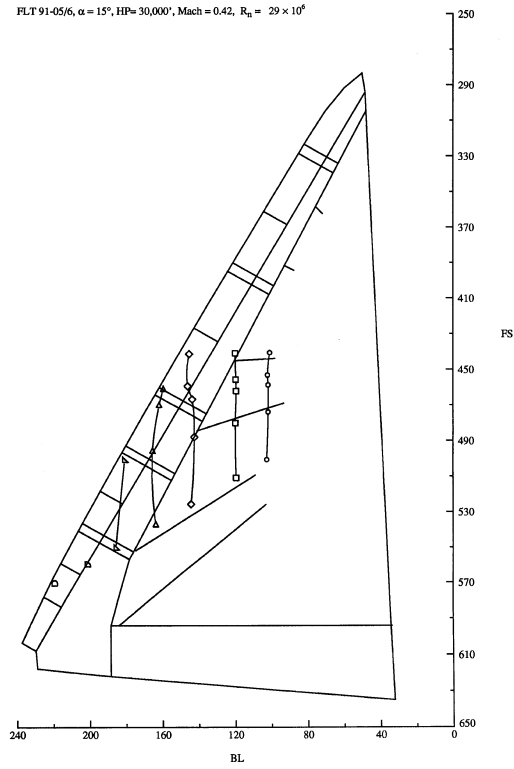


Figure 31(b) - Vortex paths, $\alpha = 15^\circ$, 40° vortex flaps, $Re = 29 \times 10^6$, Mach = 0.42.

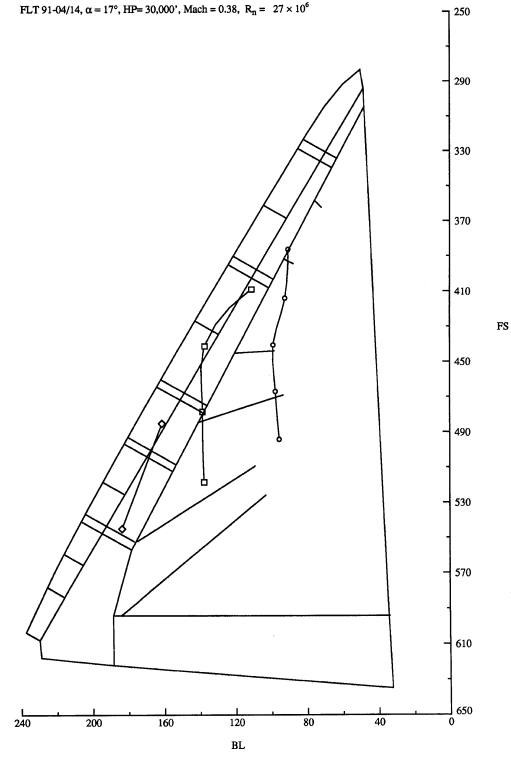


Figure 32(b) - Vortex paths, $\alpha = 18^\circ$, 40° vortex flaps, $Re = 27 \times 10^6$, Mach = 0.38.

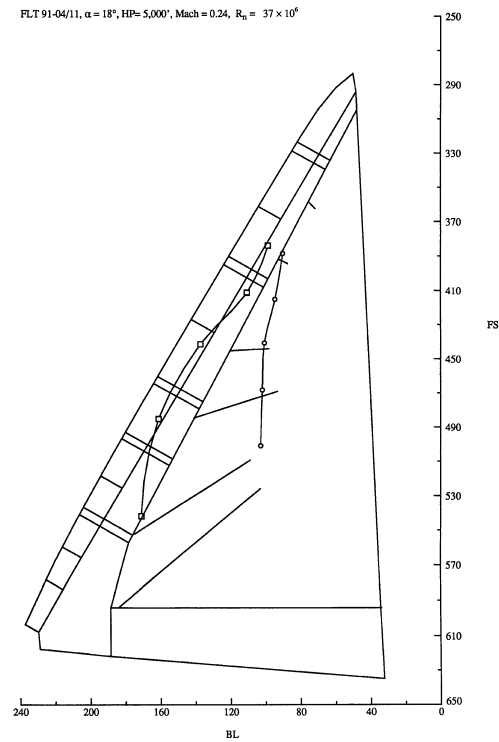
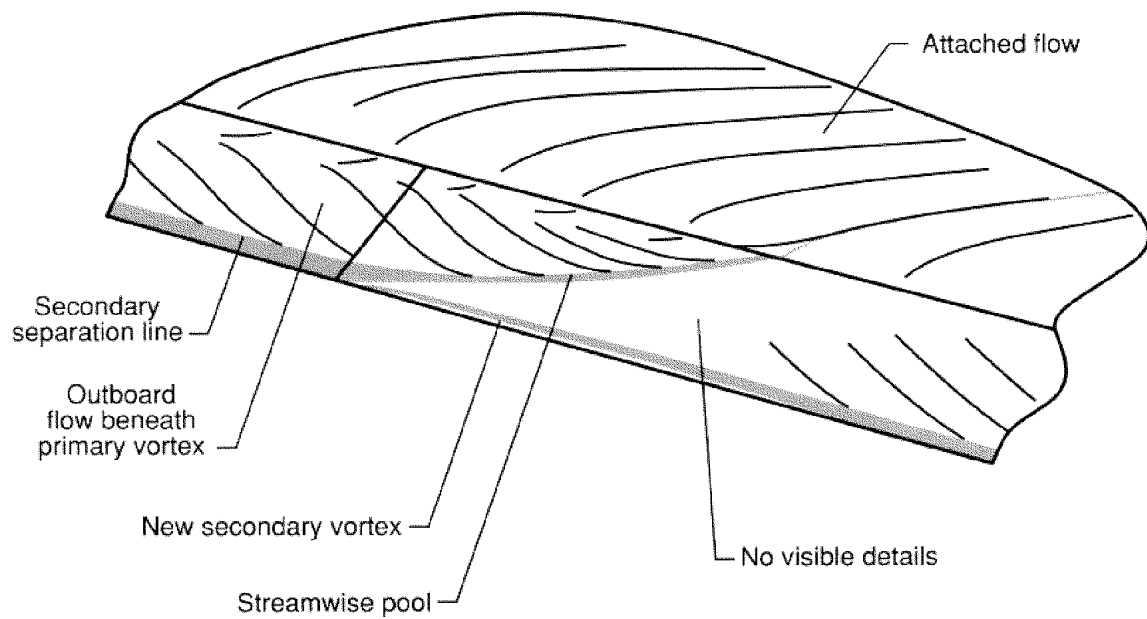
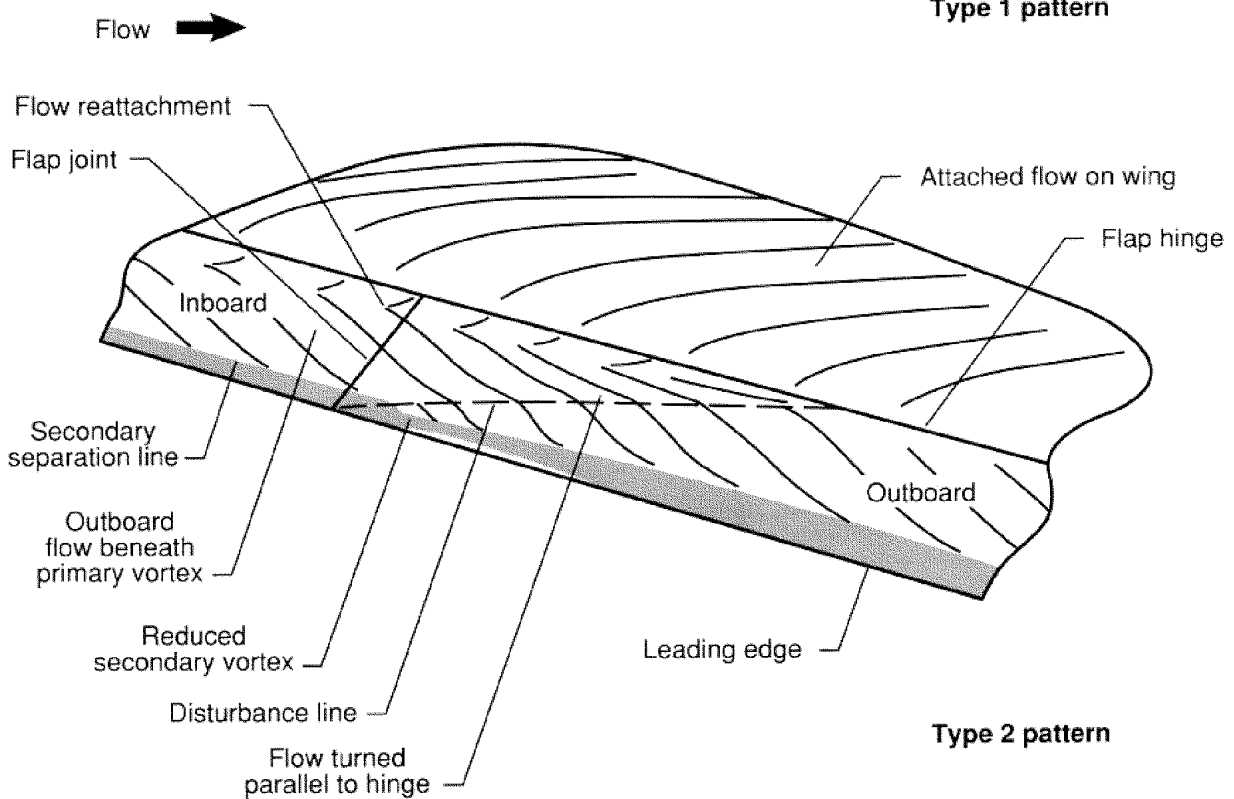


Figure 32(a) - Vortex paths, $\alpha = 18^\circ$, 40° vortex flaps, $Re = 37 \times 10^6$, Mach = 0.24.



Type 1 pattern



Type 2 pattern

Figure 33. – Flowfield sketch

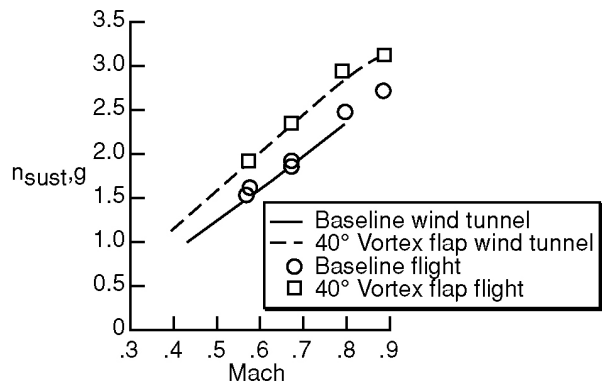


Figure 34. – Sustained load factor at maximum power, altitude = 30,000 ft

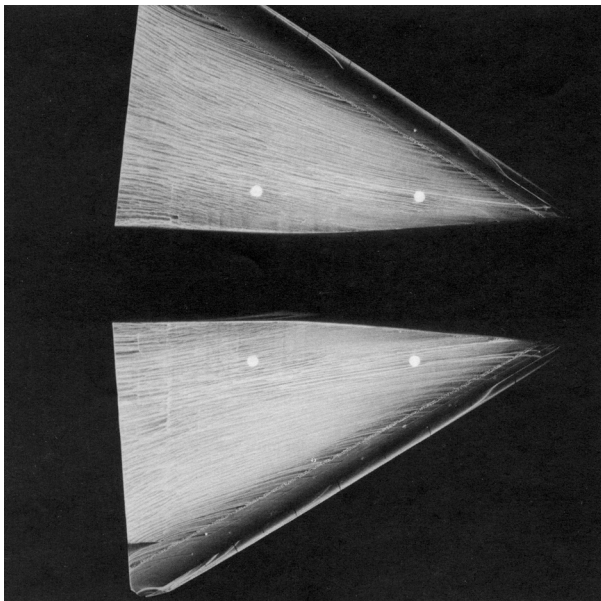


Figure 35. – Original oil flow results in tunnel investigation, $\alpha = 11^\circ$.

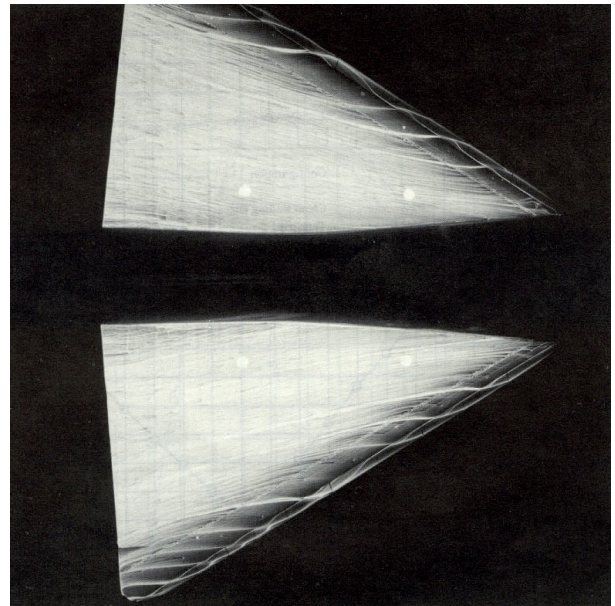


Figure 36. – Oil flow results with trips corresponding to flap segment locations, $\alpha = 11^\circ$